https://doi.org/10.5194/egusphere-2026-3615
Preprint. Discussion started: 13 July 2026

Altimetric Ku-band Radar Observations of Snow on Sea Ice Simulated with SMRT

Julien Meloche[1], Melody Sandells[2], Henning Löwe[3, †], Nick Rutter[2], Ghislain Picard[4], Richard Essery[5], Randall K. Scharien[6], Alexandre Langlois[7], Matthias Jaggi[3], Josh King[1,†], Peter Toose[1], Michele Scagliola[8], Jérôme Bouffard[8], Alessandro Di Bella[8], and Christian Haas[9]

[1]Climate Research Division, Environment Climate Change Canada, Toronto, Canada
[2]Department of Geography and Environmental Sciences, Northumbria University, Newcastle-Upon-Tyne, UK
[3]WSL Institute for Snow and Avalanche Research SLF, Davos, Switzerland
[4]Univ. Grenoble Alpes, CNRS, IGE, 38000 Grenoble, France
[5]Department of Geosciences, University of Edinburgh, Edinburgh, UK
[6]Department of Geography, University of Victoria, Victoria, Canada
[7]Département de géomatique appliquée, Université de Sherbrooke, Sherbrooke, Canada
[8]ESA-ESRIN, Frascati, Italy
[9]Sea Ice Physics, Alfred-Wegener-Institut, Bremerhaven, Germany
[†]deceased

Correspondence: Julien Meloche (julien.meloche@ec.gc.ca)

Abstract. Radar altimetry provides sea ice thickness estimates for polar region. However, uncertainty in the scattering horizon used to retrieve sea ice thickness arises from interactions between the emitted signal and snow cover on the ice surface. Therefore, improving our knowledge on electromagnetic waves scattering with the snowpack and ice is necessary to retrieve sea ice thickness accurately. The Snow Microwave Radiative Transfer (SMRT) model was used to simulate the low-resolution altimeter waveform echo from snow-covered sea ice, using in-situ measurements as input. In-situ measurements from four field campaigns in three distinct Canadian Arctic regions includes temperature, salinity, density, specific surface area, microstructure from X-ray tomography and surface roughness measurements using structure from motion photogrammetry. Evaluation of SMRT in altimeter mode was performed against CryoSat-2 waveform data in pseudo-low-resolution mode. Simulated and observed waveforms showed good agreement, although it was necessary to optimize the snow and sea ice roughness. In addition, simulations of backscatter in low-resolution mode in preparation for the European Space Agency's CRISTAL mission indicated that the dominant return comes from the ice surface at Ku-band and from the snow surface at Ka-band for smooth first-year ice. However, for rougher multi-year ice, the main scattering comes from the snow surface for both Ku and Ka-band. These findings depend on the parameterisation of the roughness. This work offers insight into the dominant surface return for Ku and Ka and paves the way towards a physical retracker using SMRT to retrieve snow depth and sea ice thickness for radar altimeter missions.

https://doi.org/10.5194/egusphere-2026-3615
Preprint. Discussion started: 13 July 2026

1 Introduction

Sea ice and snow in polar regions are key components in Earth surface energy balance. The high albedo from snow on sea ice reflects most of the solar energy and keeps the ocean from warming. The reduction of sea ice due to a warmer climate (Mudryk et al., 2018; Serreze and Meier, 2019; Richter-Menge et al., 2017) modifies the surface energy balance and creates a strong positive feedback on surface temperature (Goosse et al., 2018; Serreze and Barry, 2011). Improving measurements of cryospheric parameters such as sea ice and snow thickness on large scales is therefore a key objective in monitoring a changing climate. Sea ice thickness data can also be assimilated in meteorological models to perform seasonal forecasts of sea ice extent (Blockley and Peterson, 2018; Allard et al., 2018). Radar altimetry is a useful tool to monitor sea ice thickness over polar environments by measuring the ice freeboard. However, snow properties such as thickness and density are necessary to infer total sea ice thickness for this measurement, through the buoyancy principle and assuming hydrostatic equilibrium (Ricker et al., 2014). Moreover, surface properties such as roughness, salinity, density, temperature, and microstructure of snow and sea ice affect the accuracy of retrieval by modifying the measured radar waveform (Nandan et al., 2020; Landy et al., 2020).

Radar altimeters measure surface elevations using the two-way travel time of the emitted and reflected waves from the surface. A waveform (measurement of returned power over time) is used to analyse the reflected signal from the surface that comes from multiple facets (faces of a surface with different orientations) within the sensor footprint. The range to the surface is represented by the return of the facets at nadir as the track-point (Quartly et al., 2019). The track-point is defined on the leading edge portion (rise in power) of the waveform based on different thresholds, usually from 50 to 95% depending on the surface properties (Ricker et al., 2016), in order to estimate the range with the track-point correctly. This process is referred to waveform "retracking" with either an empirical or physical basis. Empirical retrackers are more computationally efficient and rely solely on obtaining a robust estimate of the range. Physical retrackers model the physical interaction between the transmitted pulse and the scattering surface (Quartly et al., 2019) to model SAR waveform and complex surfaces like Multi-Year Ice (MYI), First Year Ice (FYI) and leads (Dinardo et al., 2018; Landy et al., 2019).

One mathematical model of pulse-limited altimeter behaviour is given in Brown (1977). The Brown (1977) model works well for surface-dominated reflected echos such as on the ocean and land ice (Hayne, 1980; Ferraro and Swift, 1995). This formulation is not typically used for sea ice because it cannot model adequately specular reflection from leads (Landy et al., 2019) or smooth FYI. FYI can have a steeper trailing edge decay and different Pulse Peakiness (PP) which can be used to discriminate with MYI (Fredensborg Hansen et al., 2021). This is partly due to FYI being newly formed ice and smoother than older MYI or deformed FYI and therefore has waveform characteristics that correspond to a specular reflection like leads (open flat ocean) with higher PP and faster decay.

Physical retrackers are based on electromagnetic theory to model the interaction of radar signals with the surface (Wingham et al., 2004). Backscattering contributions from the surface (snow and ice) affect the waveform and therefore the retrieval of the ice thickness. Kwok (2014) simulated a height correction factor as a function of snow depth using a single layer of snow with a rough snow-ice interface. Nandan et al. (2017) and Nandan et al. (2020) added more complex snow properties and snow salinity to the correction factor. This was done by using a permittivity model for snow that accounts for dry/wetness, density

https://doi.org/10.5194/egusphere-2026-3615
Preprint. Discussion started: 13 July 2026

and brine concentration. They all found that snow properties affects the detection of the ice surface by shifting the scattering horizon of the surface upwards from the snow-ice interface. Kurtz et al. (2014) simulated a full waveform of CryoSat-2 in SAR mode rather than the Brown (1977) pulse-limited altimeter (pseudo Low Resolution Mode - pLRM for CryoSat-2), and included leads as a separate surface type. Physical retrackers like the CryoSat-2 WaveForm Fitting method (CS2WfF) (Kurtz et al., 2014) and SAMOSA+ (Dinardo et al., 2018) have added a parameter to model peaky waveforms over specular surfaces. However, they neglected the effect of snow cover and assumed the reflection coming strictly from the snow-ice interface. Fons and Kurtz (2019) improved this model by adding a snow scattering layer for Antarctic sea ice thickness retrieval. Landy et al. (2019) provided the most complete model of both SAR and pLRM mode for sea ice by incorporating roughness at two scales (footprint and radar) with a multiple facet numerical approach and the Integral Equation Model (IEM) for surface scattering. Two parameters (s and l) define the interaction of electromagnetic waves at the radar scale, where snow and ice roughness are comparable to, or less than the wavelength (2.2 cm for CryoSat-2). Previous values measured on FYI and MYI by a radar-scale LIDAR experiment s_{ice} ranged from 1 to 6 mm depending on the detrending procedure (Landy et al., 2015). The footprint-scale (or kilometer-scale) roughness varies from 1 to 100 cm and considers melt hummocks, pressure ridges, or other large-scale deformation of the ice surface. They also added volume scattering of snow using the Mie scattering theory for spherical ice particles, neglecting dense media effects (Tsang et al., 2007; Picard et al., 2022), and assumed a single grain size and no volume scattering from brine. The facet-based model lacks a complete representation of complex snow microstructure (Sandells et al., 2022) and solution of the radiative transfer equation.

Snow depth and density are key variables for sea ice thickness retrieval because snow weighs down the ice affecting its buoyancy, lowering its freeboard. Therefore, it is important to retrieve both snow depth and ice freeboard from satellite observations. Snow depth retrieval may be possible from the range difference at Ku and Ka-band (Guerreiro et al., 2016; Lawrence et al., 2018) under the assumption that the scattering horizons (track-point) are located directly at the ice surface for Ku band and at the snow surface for Ka band. However, since snow properties affect the Ku-band (Nandan et al., 2020; Landy et al., 2019) and in-situ radar observations on sea ice reveal strong power returns from the snow surface (Willatt et al., 2023, 2025), the assumption of scattering purely at the ice surface must be challenged. Investigating the scattering of Ku and Ka-band altimeter signals with a radiative transfer model that accounts for multiple layers, complex snow microstructure, wet snow, salinity, sea ice properties and rough interfaces is needed. The Snow Microwave Radiative Transfer (SMRT) model is a state-of-the-art radiative transfer model of multi-layered snow and ice at microwave frequencies (Picard et al., 2018) that allows such an investigation.

The Altimetric Ku-Band Radar Observations Simulated with SMRT (AKROSS) project was designed to provide the first evaluation of the SMRT model in altimeter mode for snow on sea ice. This model was extended to include a time-dependent radiative transfer solver for altimetry by Larue et al. (2021) and evaluated at S-, Ku- and Ka-band for ENVISAT, AltiKa and Sentinel-3A over the Antarctic Ice-Sheet. SMRT has been mostly evaluated over land (Vargel et al., 2020; Sandells et al., 2022), ice-sheets (Larue et al., 2021; Picard et al., 2022) and lake ice (Murfitt et al., 2022, 2023). Sea ice layers were added to SMRT in 2018 but evaluation of SMRT over sea ice has only been performed recently for passive microwave sensors Soriot et al. (2022). These authors used SMRT to classify snow on sea ice with passive and active microwave signatures and recently

https://doi.org/10.5194/egusphere-2026-3615
Preprint. Discussion started: 13 July 2026

SMRT was evaluated with passive microwave observations over sea ice at L-band (Fan et al., 2023). Here, we present the first study that provides SMRT forward model evaluation against altimetric satellite observations of snow on sea ice using in-situ snow microstructure measurements as input and provide insight on the radar return with perspective to retrieve snow depth for the Copernicus Polar Ice and Snow Topography Altimeter (CRISTAL) (Kern et al., 2020; Landy et al., 2026).

The purpose of this paper is to evaluate SMRT for altimetry over sea ice by 1) evaluating the overall fit of the waveform with observation of CryoSat-2, 2) investigating the sensitivity of the Ku and Ka bands to snow and sea ice parameters, and the power contribution from the surface in preparation for the CRISTAL mission.

2 Methods

2.1 Study Site

Four different datasets were used for evaluation of SMRT in altimeter mode of snow on sea ice. The field sites are located in the Arctic Ocean and in the Canadian Arctic Archipelago, as shown in Figure 1. Ground campaigns in 2016 and 2017 were associated with CryoVex and Operation IceBridge airborne campaigns. Ground campaigns in 2022 were associated with the AKROSS project and Environment and Climate Change Canada's evaluation of NASA's Ice, Cloud and land Elevation Satellite (ICESat-2) products in the Canadian Arctic. The sites observed in 2017, referred to as Alert-17 in this paper, are located in the Arctic Ocean north of Alert, Nunavut, Canada and are over MYI. Measurements made in 2016 and 2022 were located in Eureka Sound, and Cambridge Bay in the Canadian Arctic Archipelago, referred to as Eureka-16, Eureka-22 and CB-22 in this paper. Eureka-16 was characterised by FYI conditons with some localized MYI floes (Figure 1). The Eureka-22 and CB-22 were only FYI conditions. Sentinel-1 images in Figure 1 highlight the varying backscatter from local ice conditions. Pulse limited footprint centre points of CryoSat-2 observations from the temporally closest overpass dates to the in-situ measurements are also shown in Figure 1 by hollow red circles (1.6 km in diameter), with the location of in-situ observations either located within the CryoSat-2 footprint (CB-22), or located within 40 kilometers on similar sea ice types illustrated by blue (FYI) or purple (MYI) solid circles. All campaigns were carried out in April, with recorded average air temperatures of -27.8°C for Eureka-16, -22.0°C for Alert-17, -21.9°C for CB-22 and -25.2°C from Eureka-22.

2.2 Data

Table 1 provides a complete list of in-situ measured variables recorded during each field campaign. Measurements of snow density, specific surface area (SSA), temperature, salinity, and stratigraphy were made in vertical profiles in a snow pit at multiple locations, during each field campaign. For density and SSA, two vertical profiles of measurements were made in each snow pit, following the protocols discussed and illustrated in (Tsang et al., 2022), Figure A1b.

Snow samples from within the same vertical profile layer as the density and SSA measurements were bagged and labeled in the snowpit, and then brought back to the research facilities where they were melted and subsequently measured for salinity using the EcoSense EC300A conductivity meter. Salinity was measured in melted samples of snow extracted from the same

https://doi.org/10.5194/egusphere-2026-3615
Preprint. Discussion started: 13 July 2026

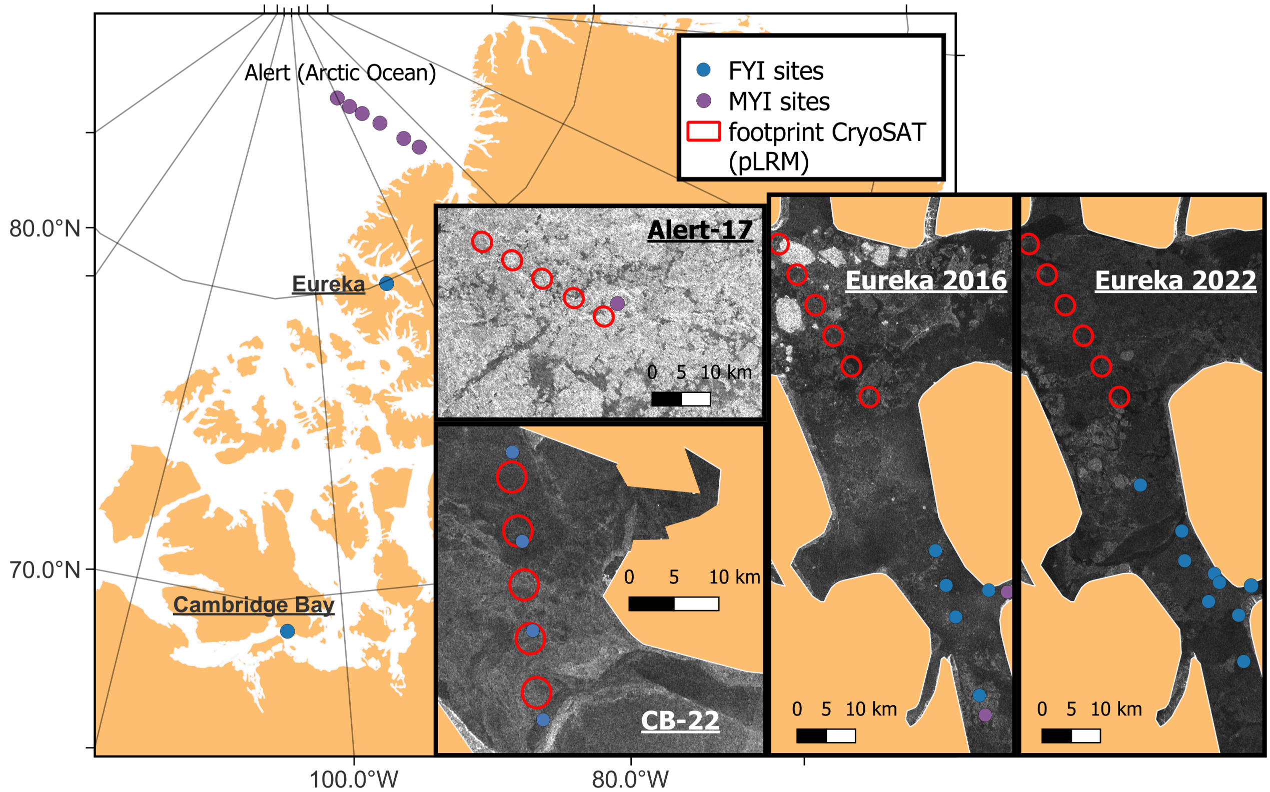

Figure 1. Location of Alert, Eureka, and Cambridge Bay (CB) evaluation field sites. Inset shows Sentinel-1 images in HH pol (CB: 2022-04-24, Alert: 2017-04-30, Eureka: 2016-04-15 and 2022-04-21) to show ice conditions at each site, bright regions correspond to MYI conditions. Locations of in-situ sites (FYI and MYI) and CryoSat-2 observations are shown.

vertical positions in the profile as density measurements. Distributed snow microstructure information (stratigraphy, derived density and SSA) was measured during all field campaigns using a Snow Micropenetrometer (SMP). In total, 809 SMP profiles were recorded on Arctic sea ice for all four field campaigns (Total snowpit coincident SMP sites: 20 in Eureka-16, 6 in Alert-17, 19 in Eureka-22, 4 in CB-22). In addition to collecting SMP profiles at snowpit locations, transects around each snowpit with varying horizontal spacings were established to characterize variations in density, SSA and stratigraphy at spatial scales of up to 100 m following similar protocols as described in Tsang et al. (2022) Appendix A1a, and illustrated in Figure A1b. An average of 69 SMP profiles were collected at each snow survey site in Eureka-16, 11 SMP profiles in Alert-17, 31 SMP profiles in CB-22 and 9 SMP profiles in Eureka-22. The Eureka-22 campaign did not follow the same SMP spatial sampling

https://doi.org/10.5194/egusphere-2026-3615
Preprint. Discussion started: 13 July 2026

Measurement	Eureka-16	Alert-17	Eureka-22	CB-22
Snow pit stratigraphy	-	-	x	x
Magnaprobe depth	x	x	x	x
Snow cutter density profiles (sampler 100 cm^3)	x	x	x	x
Snow MicroPenetrometer	x	x	x	x
SSA from snow integrating sphere (IceCube/IRIS)	-	-	x	x
Micro-CT microstructure	-	-	-	x
Snow temperature	x	x	x	x
Surface roughness from photogrammetry	-	-	x	x
Ice thickness (in-situ)	x	x	x	x
Ice / snow salinity	x	x	x	x
CryoSat-2 overpass	x	x	x	x

Table 1. Overview of available data for SMRT evaluation. x: data available, -: not observed. 2016 data reported in King et al. (2020), 2017 data reported in Haas et al. (2017).

protocols as the other campaigns, and instead surveyed spatial variability in narrower transects along 10's of kilometers of ICESat-2 satellite ground tracks.

In addition to the SMP measured snow microstructure (SSA), an integrating sphere was used to measure SSA in Eureka-22 and CB-22, respectively. Also, X-ray tomography (micro-CT) measurements were recorded during the CB-22 campaign. The vertical resolution of the SMP derived density and SSA depends on the window size used in the derivation of SMP coefficients, which was 5 mm in this case. The snow density (ρ) and SSA of the SMP were then calculated as:

$$\rho_{\text{smp}} = a_1 + a_2 \ln\left(\tilde{F}\right) + a_3 \ln\left(\tilde{F}\right) L + a_4 L \quad \text{(1a)}$$

$$SSA_{\text{smp}} = \exp(b_1 + b_2 \ln(L) + b_3 \ln\left(\tilde{F}\right)) \quad \text{(1b)}$$

where $\tilde{F}$ is the median of the penetration resistance force and L is the mean distance between structural elements in 3D space (Löwe and van Herwijnen, 2012). Coefficients are a_1 = 312.54, a_2 = 50.27, a_3 = -50.26 and a_4 = -88.15, from King et al. (2020) and b_1=2.37, b_2 =-0.7 and b_3 =-0.06 from Montpetit et al. (2024). Density coefficients from King et al. (2020) were used to derive the density profile. For SSA, as no independent SSA observations were made for Alert-17 and Eureka-16, leading to an insufficient amount of measurements to retrieve SSA coefficients, Arctic SSA coefficients were derived from the Montpetit et al. (2024) dataset over terrestrial snow in Trail Valley Creek, Inuvik, Canada, following the methodology of King et al. (2020). Similarity between SMP density coefficients of the terrestrial and sea ice snow types suggested that the transferability of SSA coefficients is also a reasonable assumption.

From the SMP profiles, a rolling median window of 3 cm was applied to produce layers of 3 cm for SMRT. For sensitivity tests, 1 cm and 5 cm rolling medians were also used in section 3.3. Layers in SMRT should not be much smaller than the

https://doi.org/10.5194/egusphere-2026-3615
Preprint. Discussion started: 13 July 2026

wavelength of the signal (Picard et al., 2018), which is ≈ 2.2 cm for Ku-band and ≈ 0.8 cm for Ka-band assuming the speed of light in air. Under these assumptions, the main layers are captured, but high-resolution features such as thin ice crusts may be missed. SMP measurements do not always capture the full profile of the snowpack as the penetration depth is manually set to sample less than the total snow depth to protect the sensitive tip from damage at the ice surface. Simulations capture the full depth of the snow profile by matching the depth measured and the SMP depth by extending the SMP profile with the last value by any additional depth. Figure 2 shows boxplots of the snow depth, density and SSA measured during the four field campaigns. Snow was deepest at the Alert-17 MYI site and also had the lowest median SSA. Eureka-22 and CB-22 were the shallowest and most dense snow, with comparable SSA to Eureka-16.

During the CB-22 campaign, snow samples were drilled in the field for micro-CT scanning following procedures from MOSAiC (Nicolaus et al., 2022) and transported from Cambridge Bay to Davos within 4 days in strict isothermal conditions at -21°C, to be scanned at the WSL Institute for Snow and Avalanche Research SLF. For the present work, only uncasted samples were used. Non-intact portions of the samples were identified after micro-CT scanning and discarded from the analysis. A CB-22 snow profile typically consists of 2 samples (height ≈ 10 cm) that was scanned and analyzed in moving window mode following standard means (Sandells et al., 2022). Density and microstructure model parameters for SMRT (Picard et al., 2018) were derived as profiles with vertical resolution of ≈ 0.8 cm that were used for the simulations presented in section 3.3. In total, four snow profiles (referred to as AK1-4 henceforth, representing the blue spots from North to South in Figure 1) were analyzed in this way.

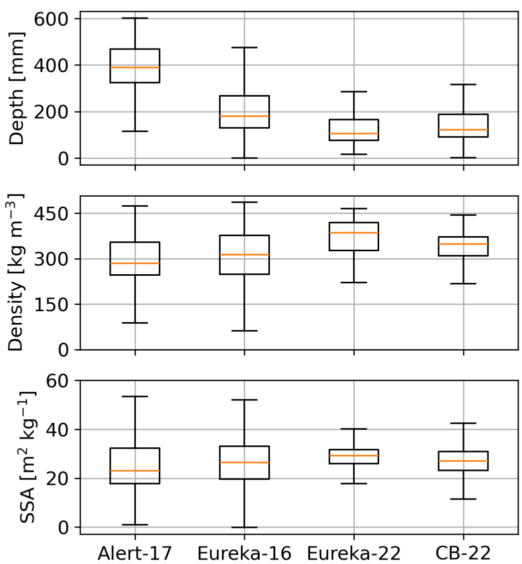

Figure 2. Box plot of SMP parameters derived from profile for Alert-17, Eureka (16 FYI only and 22) and CB-22. Density and SSA are derived from coefficients from King et al. (2020) and Montpetit et al. (2024).

https://doi.org/10.5194/egusphere-2026-3615
Preprint. Discussion started: 13 July 2026

Measured radar-scale (scale similar to the radar wavelength) roughness parameters were determined from in-situ photogrammetry recorded during the CB-22 and Eureka-22 campaigns, using the Structure from Motion (SfM) technique as described in Meloche et al. (2021). First, an area to photograph was determined to quantify the snow roughness. Then, for the same area, the snow was carefully removed by shovel to leave only the ice surface. For the processing, 3D point clouds were created for both snow and ice surfaces, and roughness parameters could be calculated, but the method deviated from Meloche et al. (2021) because the sites measured varied in area 2-4 m^2, compared to 0.5 m^2 for Meloche et al. (2021). The average point cloud density is approximately 1 points/mm^2. Following a similar procedure from Landy et al. (2015), the full area was detrended from curvature or large height deviation by sub sampling (n = 20) smaller areas and applying the same measurement procedure of fitting a plane to this subset. Each subset will fit a different local plane. The height standard deviation was calculated with respect to the local plane of each subset. The correlation length was estimated using the autocorrelation function of heights. The mean for all subsets was used to estimate both roughness parameters. Two point clouds were created from in-situ photogrammetry at every site for the snow surface and the sea ice surface. In total, 8 surfaces were used to derive roughness parameters for snow and 8 for sea ice surfaces.

2.3 Simulation Framework

2.3.1 Snow Microwave Radiative Transfer (SMRT) model

The SMRT model was adapted for low-rate mode altimeter applications by Larue et al. (2021). SMRT is a multilayer model, with each snow layer represented by temperature, density, thickness and microstructure parameters. The layers are separated by interfaces, which are flat (i.e. reflectivity is calculated with Fresnel equations) by default but rough interfaces may also be specified. Beneath the snow, ice layers may be specified with different parameters: type (fresh, first year or multiyear sea ice), temperature, density, thickness, microstructural parameters and salinity. First year sea ice is represented as brine scatterers within a pure ice background, whereas multiyear ice is represented as air bubble scatterers within a slightly saline ice background. The medium beneath the lowest layer (called substrate in SMRT) can be represented in a variety of ways: by permittivity or reflectivity. For the simulations presented here, the substrate is water with a flat interface.

Input parameters are used with the permittivity model to calculate the electromagnetic properties i.e. scattering and absorption coefficients and phase functions. These parameters depend on which electromagnetic model is used,e.g. Improved Born Approximation (IBA) or Dense Media Radiative Transfer model with Quasi-Crystalline approximation (DMRT-QCA). The electromagnetic parameters are then used with the interface boundary conditions to solve the radiative transfer equation. SMRT was originally developed with a discrete ordinates radiative transfer solver (DORT), which enabled simulation of brightness temperature for passive mode and backscatter for active mode (Picard et al., 2018). Extension of SMRT for altimeter applications uses the existing SMRT core infrastructure to construct the medium and calculate its electromagnetic properties. However, simulation of the waveform is then performed via the time-dependent radiative transfer solver outlined in Larue et al. (2021) instead of DORT. Receiving antennas sample the incoming signal at discrete time intervals called gates or bins. Penetration of the signal into the snowpack is taken into account, as well as the delay implied by the horizontal extent of the beam,

https://doi.org/10.5194/egusphere-2026-3615
Preprint. Discussion started: 13 July 2026

but returns from elsewhere within the beamwidth at a particular time will be from lower depths for nadir return, as illustrated by the blue grid in Figure 1b from Larue et al. (2021). These grids are combined to form a series of thinner layers in SMRT for the calculation. The width of the gate depends on the pulse bandwidth. For CryoSat-2 the pulse bandwidth is 320 MHz, which means the altimeter gate sampling rate Δt is 3.125 nanoseconds. For LRM waveforms (only waveforms currently implemented in SMRT), the returned power is then calculated:

$$P_r(t) = pdf(t) * P_{\mathrm{FS}}(t) * [\sigma_{\mathrm{s}}((\theta(t)) + I_{\mathrm{int}}(t) + I_{\mathrm{vol}}(t)] * P_{\mathrm{T}}(t) \tag{2}$$

as the convolution of the sum of intensities (equation 9,12,13 in Larue et al. (2021)) with the waveform functions; the flat-surface impulse (P_{FS}), a probability density function of the surface ($pdf(t)$) and the transmitted signal power (P_{t}). For full details of the solution method, see Larue et al. (2021).

Separation of the different backscatter components (surface, interface and volume) in equation 2 means that it is possible to calculate their relative contributions. The three additive components: (σ_{s}, I_{int}, I_{vol}) the surface, interface and volume specific intensities are calculated from components of SMRT such as permittivity models for snow and ice, microstructure representation and electromagnetic models to calculate the scattering and absorption coefficients which are determined by the snow and ice stratigraphic and physical properties such as temperature, density, grain size (microstructure), liquid water content and salinity.

The backscattering coefficients of the surface and interface (σ^0_{s} and σ^0_{int} - equation 13 in Larue et al. (2021)) represent the incoherent reflections in Larue et al. (2021). Since this study focuses on sea ice rather than ice sheet, the coherent component needs to be accounted for because some ice types are quasi-specular (De Rijke-Thomas et al., 2023). Both coefficients are now the addition of both the incoherent and coherent effects ($\sigma^0 = \sigma^0_{\mathrm{incoh}} + \sigma^0_{\mathrm{coh}}$). The incoherent part is calculated with the surface scattering model, Integral Equation Model (IEM) or Geometrical Optics (GO) model, given the relevant roughness parameters (depending on the model used). The radar-scale roughness is defined by the root-mean-square of height (s) and the correlation length (l). The radar-scale roughness is defined in this paper with a subscript of ice or snow (i.e s_{ice} or s_{snow}) depending on the surface they refer to. Both surface scattering models, IEM and GO, were used depending on the scale domain (for IEM: $ks <$ 3 and GO: $ks \gg 1$ where k is the wavenumber). GO was also used in the Ka-band study for the surface roughness since ks was larger than 3. The coherent part is define in De Rijke-Thomas et al. (2023) (equation 5.1) by :

$$\sigma^0_{\mathrm{coh}} = \frac{\left|\Gamma(\theta)\right|^2}{\frac{1}{k^2h^2\beta^2} + \frac{\beta^2}{4}} \exp\left[-4k^2s^2 - \frac{\theta^2}{\frac{1}{k^2h^2\beta^2} + \frac{\beta^2}{4}}\right] \tag{3}$$

with $\Gamma(\theta)$ define as the Fresnel reflection coefficient, h is the distance from the satellite to the surface, β is the beamwidth of the radar.

For the waveform model, spherical propagation of the wave and pulse shape is assumed based on Brown (1977) classical radar theory. The power of a flat-surface impulse (P_{FS}) is defined here as equation 4 (or equation 14 in Brown (1977)):

$$P_{\mathrm{FS}}(\tau) = \frac{G_0^2\lambda c}{4(4\pi)^2h^3} \cdot \exp\left[-\frac{4}{\gamma}(\sin^2\theta + \frac{c\tau}{h\eta}\cos 2\theta)\right] \cdot J_0\left(\frac{4}{\gamma}\sqrt{\frac{c\tau}{h\eta}}(\sin 2\theta)\right) \tag{4}$$

https://doi.org/10.5194/egusphere-2026-3615
Preprint. Discussion started: 13 July 2026

with time defined as the reduced time $\tau = t - t_0$, where $t_0 = 2h/c$ is the nominal time defined as the round trip time. The effect of Earth's finite curvature is included by adding a factor of $\eta = (1 + h/R)$ where R is the Earth's radius (Larue et al., 2021). G_0 is = 1, λ is the satellite sensor wavelength of CryoSat-2 (2.2 cm), c is the speed of light, J_0 is the order zero modified Bessel function (J_0 = 1 if θ = 0) and $\gamma = 2\sin^2(\beta/2)/\ln 2$, determined from β. Modelling an asymmetric beamwidth in the along and across-track and P_T = sinc(τ) could be considered in the future to model the SAR mod from CryoSat-2 or CRISTAL. θ is the incidence angle of the beam.

A rough surface affect both the amplitude and the decay of the return. The waveform has a stronger return coming from the side lobes (off-nadir), leading to a lower amplitude and slower decay. A smooth surface has a strong return mostly from the nadir components, leading to a stronger amplitude and a faster decay. This is usually taken into account by a decrease of backscatter as a function of the incidence angle using a parametrization of radar-scale roughness in $P_\mathrm{FS}(\tau)$ (Brown, 1977; Kurtz et al., 2014; Landy et al., 2019). However, SMRT altimetry calculates the decrease of backscatter as a function of incident angle in a physical way by computing surface backscatter over different off-nadir incidence angles. To compute multiple incident angles, the theta_inc_sample parameter in SMRT was set to 64 to sample over multiple angles.

Scattering surface roughness at the footprint scale (σ_surf) is represented through a probability distribution function:

$$pdf(\tau) = \frac{1}{\sqrt{2\pi}(2\sigma_\mathrm{surf}/c)} \exp\left(\frac{-\tau^2}{2(2\sigma_\mathrm{surf}/c)^2}\right) \tag{5}$$

currently assumed to be Gaussian in SMRT LRM altimetry module. The σ_surf is the footprint-scale roughness (1 km) of the sea ice in the footprint which is different than s or l that affect surface scattering at the radar scale. Values of σ_surf are usually between 10 and 30 cm (Landy et al., 2020) and the $pdf(\tau)$ term becomes negligible under 10 cm.

The transmitted signal pulse is approximated with a Gaussian function of time:

$$P_\mathrm{T}(\tau) = \frac{1}{\sqrt{2\pi}\sigma_\mathrm{p}} \exp\left(\frac{-\tau^2}{2\sigma_\mathrm{p}^2}\right) \tag{6}$$

where Δt is the inverse of the sensor pulse bandwidth and $\sigma_p = 0.513\Delta t$ as in Larue et al. (2021); **?**.

2.3.2 Simulation Approach

Simulations of mean waveform for each location; Alert-17, Eureka-16/22 and CB-22 were compared with the mean of CryoSat-2 observed waveforms per location. All simulations use in-situ SMP measurements of snow properties as described in Section 2.3.3. Integrating Sphere and micro-CT data were not used since they were not available for all sites. This allowed snow variability from multiple snow surveys to be incorporated in SMRT simulations. As absolute power is not available, we then found the scaling factor adapted to the sensor (CryoSat-2), to compare simulated relative power to the altimeters' observation. Second, we optimized the radar-scale roughness of sea ice (s_ice and l_ice) with the backscattering coefficient per location.

2.3.3 Simulation Parameters

Snow depth, density and SSA profiles were derived from SMP observations and used to simulate a waveform for each profile. A rolling median was applied to extract density and SSA from the SMP measurements at vertical resolutions suitable for

https://doi.org/10.5194/egusphere-2026-3615
Preprint. Discussion started: 13 July 2026

SMRT input. For the simulations in this study, an exponential microstructure model was used. The modified Debye equation was used to calculate the microwave grain size (l_{mw}) using the Porod length l_{p} and polydispersity (K) following the approach from Picard et al. (2022):

$$l_{\mathrm{MW}} = Kl_{\mathrm{p}} = K\frac{4(1-\rho_{\mathrm{s}}/\rho_{\mathrm{i}})}{\rho_{\mathrm{i}}SSA} \tag{7}$$

where ρ_{s} is the snow density and ρ_{i} is the density of ice. The polydispersity was set using grain type from an SMP predicted grain type classifier (rounded, faceted or depth hoar) for snow on sea ice (King et al., 2020). K was assumed to be 0.7 for rounded and faceted and K = 1.3 for depth hoar following Picard et al. (2022). Usually, snow salinity of upper layers is minimal (< 1 PSU) and increases to 1-20 PSU for the basal layers next to sea ice (Nandan et al., 2017; Geldsetzer et al., 2009). Measured values in CB-22 were < 1 PSU for upper layers. Basal layers had an average of 9.3 $\pm$ 3.5 PSU for CB-22 and 10.6 $\pm$ 5.5 PSU for Eureka-22. Alert-17 and Eureka-16 had lower salinity with a mean basal layer of 3 PSU for Eureka-16 and 0 PSU for Alert-17. FYI has higher salinity due to brine expulsion from the sea ice where MYI snow basal layer is much fresher since the brine expulsion is flushed by melt (Nandan et al., 2017). Snow salinity increases the microwave absorption, leading to stronger attenuation and emission in saline snow than in fresh snow. Snow salinity was set to the measured values and the saline snow permittivity model from Geldsetzer et al. (2009) was used.

Sea ice scattering in SMRT is assumed to be brine scatterers within a pure ice background for first-year ice (FYI) and air bubble scatterers within a slightly saline ice background for multiyear ice (MYI). For FYI, the density of the ice is set to 910 kgm^{-3}, for MYI the density is reduced to 880 kgm^{-3} by modifying the volume fraction of air/ice (Laxon et al., 2013). For both cases, scatterers within the sea ice were assumed to be spheres of radius 1 mm. Sea ice temperature of 260 K was set for the simulation. The ice salinity was set to the measured ice surface salinity at all sites. The mean ice salinity of the different sites is found in Appendix C1. The thickness of FYI was set to 2 m and MYI was 3 m in the simulations, with a water substrate underneath both.

The roughness of snow and sea ice (Figure 3) is defined in the modelling of altimeter waveforms at two different scales: footprint-scale and radar-scale as defined in Landy et al. (2020). Roughness measurements in the CB-22 and Eureka-22 campaigns focused on roughness parameters at the radar scale. Although not evaluated for this project, some of our field measurements contained such large features that could potentially overestimate the radar-scale roughness. This will be discussed further as these features were found in our field experiment for rough sea ice (Figure 3). Footprint-scale roughness σ_{surf} represents the height standard deviation of the surface within the altimeter footprint ($upto 15$ km) assuming a probability density function for the surface (Landy et al., 2020). SMRT assumes a Gaussian distribution for the surface height and σ_{surf} = 0.14 m for FYI and σ_{surf} = 0.22 m for MYI from Table 2 in Landy et al. (2020) were used in simulations. These values were obtained from airborne radar surveys of the sea ice surface in Landy et al. (2019).

Table 2 presents mean roughness values for flat ice, rough ice and snow surfaces measured in CB-22 and Eureka-22. Figure 3 shows the bivariate distribution with parameters (s, l) for the three different surfaces and shows two distinct regions for the sea ice and similar values between flat ice and the snow surface. We would suggest that the rough ice (green dots in Figure 3) measurements with a roughness 15 times larger contribute more to the parameters σ_{surf} at the larger scale.

https://doi.org/10.5194/egusphere-2026-3615
Preprint. Discussion started: 13 July 2026

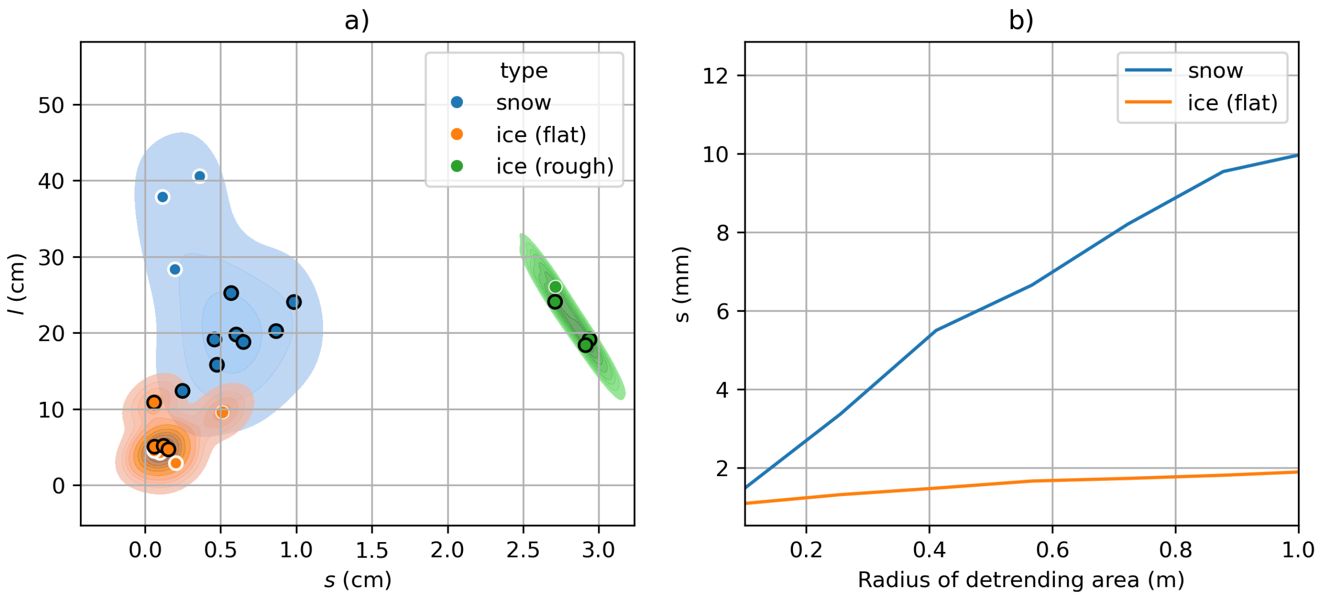

Figure 3. a) Snow surface (n = 11), b) flat sea ice (n = 9) and c) rough sea ice (n =3). d) 2D Kernel density estimate of roughness parameters measured (l, s) of the surface in a), b) and c). Black outline indicates a measurement from CB-22 and white outline for Eureka-22.

surface	s (mm)	l (cm)	n
snow	5.0 ± 1.4	23.8 ± 4.3	11
flat sea ice	1.6 ± 0.8	5.8 ± 1.4	9
rough sea ice	28.2 ± 0.6	22.0 ± 1.9	3

Table 2. Overview of the measured roughness parameters. Rough sea ice had a mean radar-scale rms (s) of 39.0 mm, snow had 5.5 mm and flat sea ice had 1.5 mm. These values were obtained with a detrend radius of 0.4 m.

2.3.4 Normalisation

SMRT simulations of the altimeter waveform provide the ratio between received and emitted powers, neglecting the atmospheric transmission and assuming an antenna gain $G_0 = 1$. To compare the satellite observations to the simulated relative power, a normalisation is necessary. A similar method to Larue et al. (2021); Legresy et al. (2005) was applied here, which is a least squares regression fit to the satellite observations. The normalisation factor (Λ) is calculated across all sites assuming the satellite calibration is constant between acquisitions. The Λ is multiplied by the simulation (unitless) to match the observation power in raw data units (integers).

In their study over Antarctica, Larue et al. (2021) were able to use data over several months (at least 50 observations at each of seven sites) due to slowly changing snow microstructure. Data were also filtered for $\pm$ 1 gate tolerance. Here, data are much more limited and only two obvious outliers in Eureka-16 that had more than 20 gates difference were excluded. For the final calculation of the normalisation factor, all observed waveforms per site were aligned to the same nominal gate (Figure D1) as the simulation, then averaged together to yield one mean waveform. This allowed a proper calculation of the normalisation factor between the simulated and observed.

2.4 Roughness Optimisation

The radar-scale roughness of snow and ice impacts the total power measured by the altimeter (equation 2). The reflection from rough surfaces is represented by IEM or GO surface models and the roughness values are key in modelling the backscatter. The radar-scale roughness was measured only for CB-22 and Eureka-22 and yielded distinct values for flat and rough ice. It is unclear whether the values measured spatially represent the true roughness. For this reason, the s and l of both the sea ice and snow are optimized per campaign (Eureka-16, Alert-17, Eureka-22 and CB-22) using a least-square fit of the residual between the observed and simulated waveforms and then compared with measured values from this study and Landy et al. (2015). To simplify the optimization, the correlation lengths of the ice and snow are assumed equal ($l_{\text{snow}} = l_{\text{ice}} = l$). Also, we focused on optimizing the radar-scale roughness since it affects the amplitude of the simulated waveform the most (De Rijke-Thomas et al., 2023). We assume flat snow interfaces and refer to the snow surface and ice surface from now on.

Since Λ influences the amplitude of the simulated power, normalisation was estimated before the optimization with first guess $s_{\text{snow}} = s_{\text{ice}} = 5\,\text{mm}$. Then, the optimized range for s was 1 to 10 mm and 1 to 100 cm for l based on Landy et al. (2019) and our measured values. The s_{ice} and s_{snow} were optimized for each site. The optimization of the waveform was based on the least squares residuals. The residuals were the difference between the observed and simulated power at each gate. To evaluate our fit, the norm squared of the residuals (n_{res}) was used as a metric. Fons and Kurtz (2019) defined a good waveform fit when (n_{res}) < 0.3. The gates 0 to 160 from the fit to reduce the influence of noise. The nominal gate is 164 at which SMRT will simulate the first surface return.

2.5 Sensitivity analysis

The aforementioned simulation setup with the SMP profiles, measured properties and optimized roughness was also used for a sensitivity analysis on snow and ice parameters in the model (Section 3.2). Three simulations per property were estimated. A reference simulation was conducted using the previously described setup, along with two additional simulations featuring a variation (e.g., $\pm$ 50% snow depth) to illustrate the impact on the waveform.

3 Results

3.1 SMRT Evaluation

In this section, the waveforms modeled by SMRT using the measured snow parameters driven from SMP measurements were evaluated at all sites. The observed waveforms from CryoSat-2 at Eureka-16/22, Alert-17 and CB-22 are shown with dashed lines in Figure 4. The amplitude of Alert-17 (MYI) was lower than the amplitude of CB-22 and Eureka-22 (FYI). Eureka-16

https://doi.org/10.5194/egusphere-2026-3615
Preprint. Discussion started: 13 July 2026

composed of a mixture of FYI and MYI has a higher amplitude than Alert-17 but lower than CB-22 and Eureka-22. The amplitude decay or the slope of the trailing edge (TES, Table 3) on the log scale showed a different decay between CB-22/Eureka-22 and Alert-17/Eureka-16, which indicates the contribution of coherent power for faster decay.

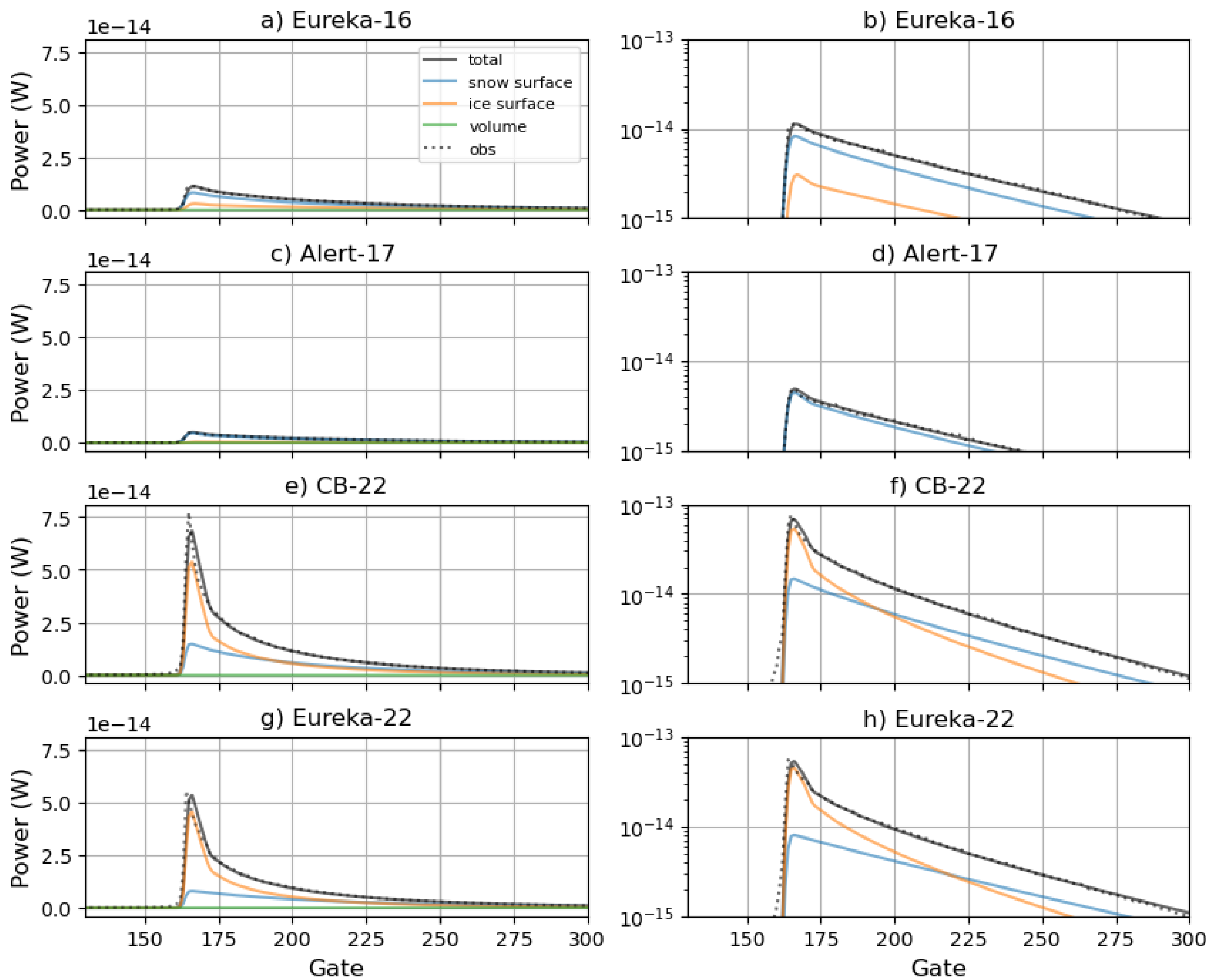

Figure 4. Comparison between simulated and observed CryoSat-2 waveforms for Alert-17, Eureka-16/22 and Cambridge Bay with a normalisation factor, 2.2×10^8. Simulated waveforms are shown by a black solid line and observation by dotted lines. The different contributions of the received power are also shown by colored solid lines. For sake of clarity, the right-hand side column is a linear scale and the left-hand side is a logarithmic scale of the power.

https://doi.org/10.5194/egusphere-2026-3615
Preprint. Discussion started: 13 July 2026

SMRT simulations of CryoSat-2 waveforms are also shown in Figure 4 for each site with the normalisation factor of $\Lambda = 2.2 \times 10^8$(Table 3). Poor fit using a constant roughness for all sites was obtained (not shown here). Optimized roughness parameters for the simulations in Figure 4 are shown in Table 3.

The optimized roughness per site (Table 3) yielded lower s values for CB-22 = 2.9 mm and Eureka-22 = 3.0 mm and rougher sea ice for Eureka-16 = 4.5 mm and Alert-17 = 5.4 mm. The l yielded the maximum value of the optimized range for CB-22 and Eureka-22. A rougher ice surface was needed for Alert-17 and Eureka-16, which is consistent with the MYI characteristics for Alert-17 and mixed MYI/FYI characteristics for Eureka-16 (Figure 1). Smoother ice for CB22 and E22 yielded a stronger return and higher peakiness due to coherent reflections. Overall, the n_{res} showed that a good fit was obtained when the roughness was optimized, but the peakiness was slightly underestimated, particularly prominent in the absolute backscatter for pure FYI sites.

Site	s_{ice} (mm)	s_{snow} (mm)	l (cm)	n_{res}	TES
Eureka-16	4.5	4.6	46	0.004	-0.018
Alert-17	5.4	3.9	22	0.003	-0.017
CB-22	2.9	5.3	100	0.02	-0.021
Eureka-22	3.0	6.4	100	0.04	-0.021
Normalisation factor: $\Lambda = 2.2 \times 10^8$					

Table 3. Overview of the optimized roughness parameters, waveforms fit parameters and the normalisation factor.

The contributions of the backscatter sources, i.e., snow surface, ice surface, and snow volume to the total backscatter were also shown. A mixture of returns from the snow and ice surface was obtained for CB-22 and Eureka-22 (FYI) and returns dominated by the snow surface for Alert-17 and Eureka-16. This means that for Ku-band, backscatter was dominated by changes in the permittivity of snow and ice layers, which increased reflectivity between layers, and the roughness of the snow and ice surface. The volume scattering response is small compared to the surface response at Ku-Band.

The simulated leading edge was investigated in Figure 5. Since no footprint-scale roughness was available, different values (0.14, 0.22 and 0.5) are shown so the assumed values from the literature for FYI (($\sigma_{\mathrm{surf}} = 0.14$) and for MYI (($\sigma_{\mathrm{surf}} = 0.22$) could be evaluated. It can be seen that 0.14 fits well the leading edge of CB-22, Eureka-22 and Eureka-16. However, Alert-17 needs a higher value than 0.22 for a better fit.

3.2 Sensitivity analysis

After optimization and evaluation of the SMRT simulated waveforms, we investigated the effect of simulation parameters on 1) the total simulated power and 2) the power contribution simulated by SMRT. First, a sensitivity analysis was carried out on the total power to identify parameter accuracy constraints. These results were shown in Figure 6 for Ku-band and Figure 7 for Ka-band, based on measured values from SMP profiles. We selected CB-22 and Alert-17 as they both were representative of FYI and MYI respectively. The mean simulations using in-situ parameters (same as Figure 4) were shown as the solid line for

https://doi.org/10.5194/egusphere-2026-3615
Preprint. Discussion started: 13 July 2026

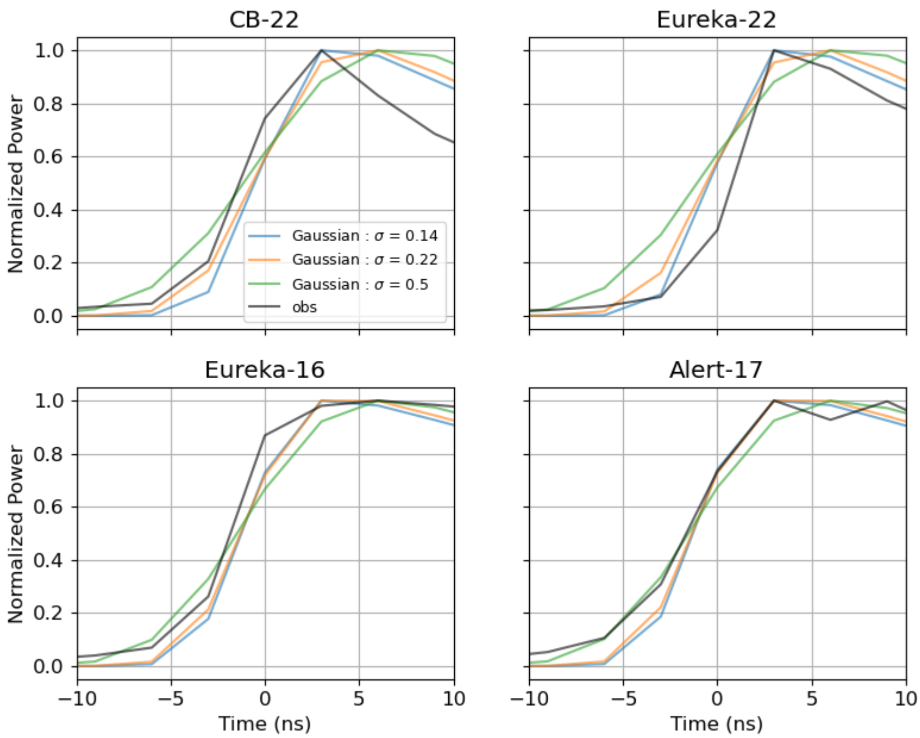

Figure 5. Simulation of the leading edge for all sites as a function of the σ_{surf}.

CB-22 and Alert-17 profiles. Parameter modifications were shown by dotted and dashed lines (reductions or increases from the measured parameters).

In Figure 6, the parameters that were used in the calculation of both snow and sea ice permittivities (snow density, snow temperature, snow salinity, sea ice salinity and sea ice temperature) all affected the amplitude. This can be noted from Figure 6 c), d) and e) because the temperature, density and salinity affect the permittivity of snow in SMRT. Snow salinity only affected CB-22 since saline snow is not present on MYI (Alert-17). In h), volume fractions (driven by brine concentration/salinity for FYI and ice density for MYI) and temperatures of sea ice had a smaller but notable impact on the amplitude. The snow parameters that most affected the amplitude were the depth, density and salinity. Snow depth did not affect Alert-17 since reflected power comes from the snow surface at this site (see Figure 4). For the roughness, it can be seen from Figure 6 f) and g) that the roughness greatly affects the amplitude. The roughness also affects the decay of the waveform. Variation in snow SSA did not effect the total amplitude at Ku-band for either site.

For Ka-band (Figure 7), a similar sensitivity to snow parameters was found. Snow depth did affect the amplitude of both sites. Again, a strong sensitivity to snow density for both CB-22 and Alert-17 was observed. For Alert-17, sensitivity to SSA

https://doi.org/10.5194/egusphere-2026-3615
Preprint. Discussion started: 13 July 2026

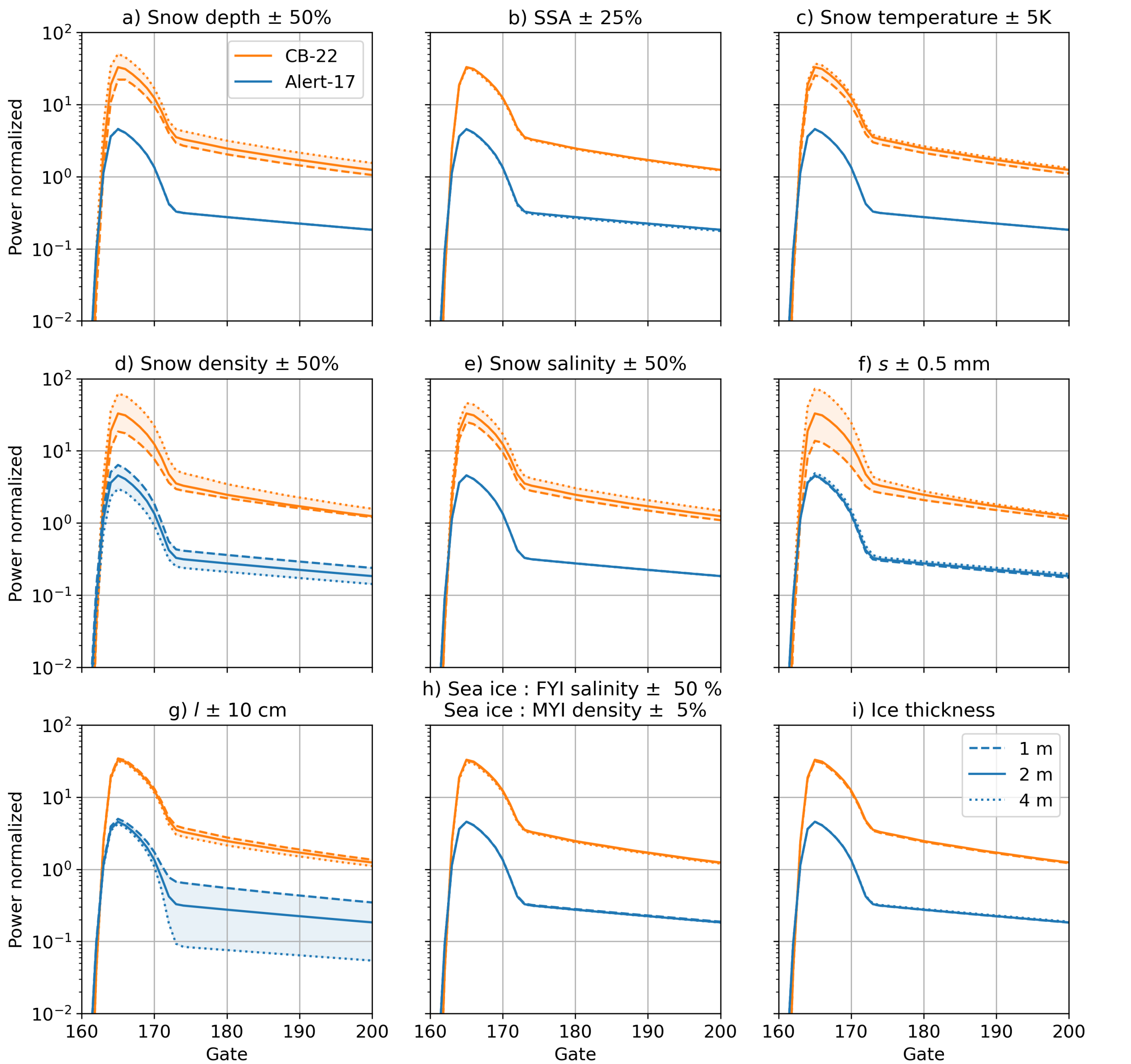

Figure 6. Ku-band sensitivity analysis around the mean measured parameters used to drive SMRT simulations for CB-22 and Alert-17. The solid line is the mean simulation, the dotted line is the negative change and the dashed is the positive change.

370 can be observed even when a negligible volume scattering contribution was simulated. This is due to the basal layer of depth hoar in Alert-17 scattering (diverging) the reflection from the ice surface, which is likely to reduce the total backscatter. This

https://doi.org/10.5194/egusphere-2026-3615
Preprint. Discussion started: 13 July 2026

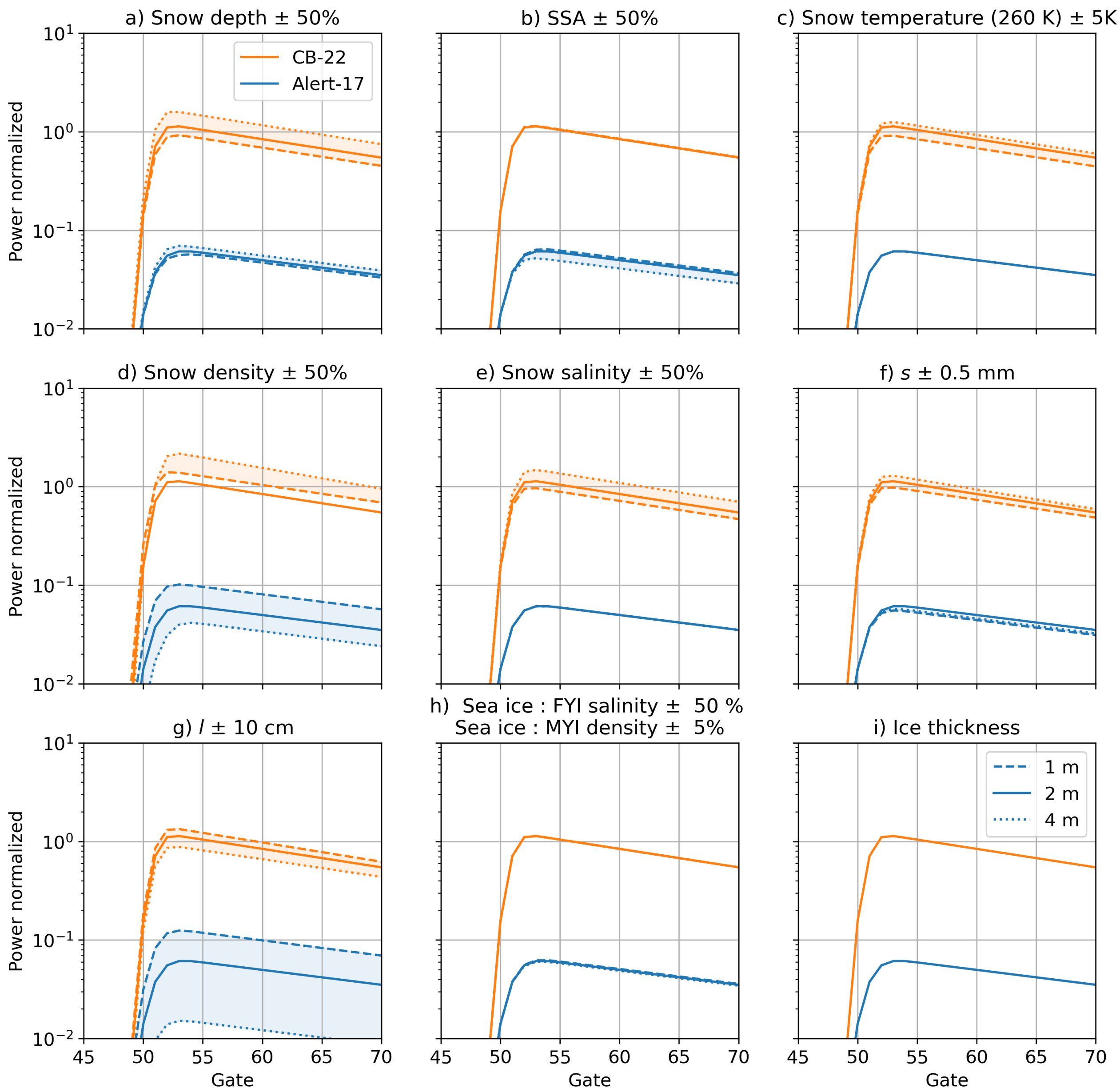

Figure 7. Ka-band sensitivity analysis around the mean measured parameters used to drive SMRT simulations for CB-22 and Alert-17. The solid line is the mean simulation, the dotted line is the negative change and the dashed is the positive change.

effect was not present at Ku-band due to a larger wavelength, where the interaction with the snow grain is diminished. Also, the shape of the waveform indicates less coherent return than at Ku-band.

https://doi.org/10.5194/egusphere-2026-3615
Preprint. Discussion started: 13 July 2026

In Figure 8, the effect of roughness parameters was investigated further by accounting for the backscatter contributions explicitly. It shows that the relative influence of surface roughness from both snow and ice on the total power depends on the radar-scale roughness. For Ku-band, ice surface contribution was dominating for low roughness ($s_{\mathrm{ice}} < 4$ mm) but surface reflection dominated as s increased ($s_{\mathrm{ice}} > 4$ mm). For Ka-band with GO, the snow surface is dominating but the ice surface was still >= 18 % for both sites. For Ka-band with IEM, the backscatter contribution from the snow volume increases to a maximum of 10% at the Alert-17 MYI site for rougher snow.

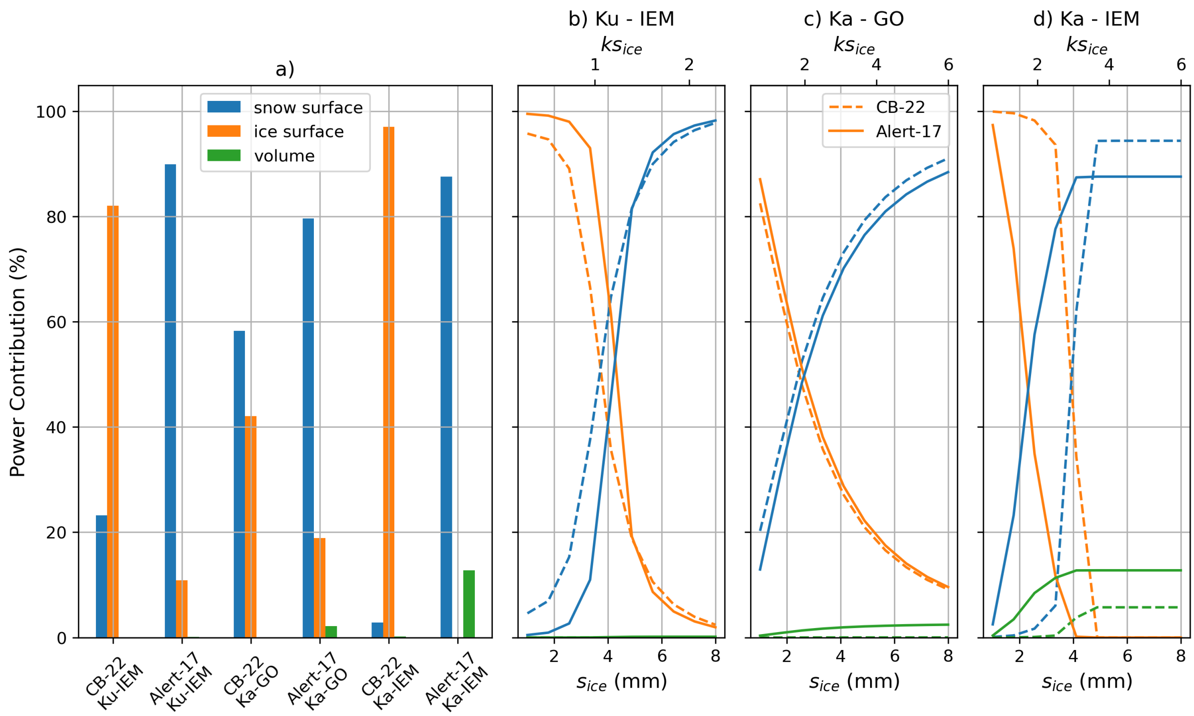

Figure 8. a) Contribution of total power from reflection of the snow surface, ice surface and volume scattering for CB-22 and Alert-17 for Ku and Ka-band. The contribution as a function of the s_{ice} is shown in b) for Ku with IEM, c) for Ka with GO and d) for Ka with IEM.

Finally, in Figure 9, the effect of the microstructure and salinity was investigated on the backscatter contributions. Here, GO was used for Ka-band and IEM for Ku-band. The SSA was varied by ± 50 % from the measured values. The backscatter contribution varied by 40 % for Ka-band at Alert-17. Again, this is because lowering the SSA of the depth hoar layer increased the divergence of the radar wave reaching the base of the snowpack which ultimately reduced the contribution of the ice surface. A similar effect is seen for salinity at CB-22 where an increase in salinity reduces the ice surface contribution. The brine in the snow absorbs the radar wave reaching the base of the snowpack which also reduces the contribution of the ice surface as salinity increases.

https://doi.org/10.5194/egusphere-2026-3615
Preprint. Discussion started: 13 July 2026

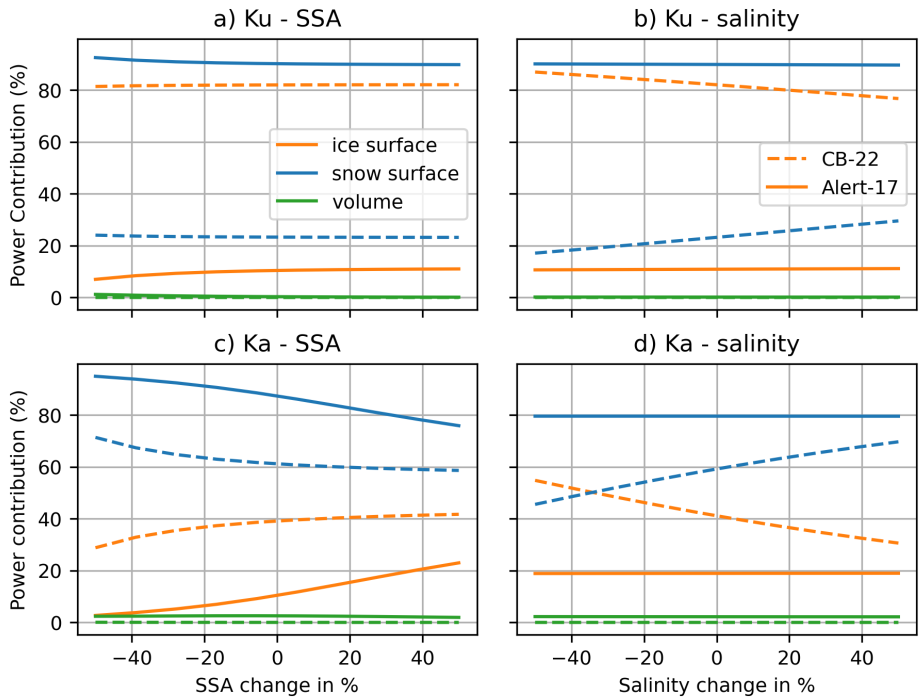

Figure 9. Sensitivity of the SSA and salinity of snow on the power contribution (%) from the snow surface, ice surface and volume scattering.

3.3 Micro-CT

We investigated how the high-resolution micro-CT measurements of snow used as inputs into SMRT affected the simulations across the 4 survey sites in CB-22 (AK1-AK4). Figure 10 a) shows the difference in measurement between the traditional pit, SMP at two different resolutions and micro-CT measurements. The varying levels of vertical resolution are: pit density cutter (3 cm), SMP rolling median window (5 cm and 1 cm), and micro-CT observations (0.8 cm). Density cutter measurements showed the least variability in ice volume fraction(ϕ = 0.4 $\pm$ 0.03), and micro-CT the greatest (ϕ = 0.37 $\pm$ 0.06). It is known that the volume fraction (snow density) measured by a CT is a more accurate representation than other measurement methods (Proksch et al., 2016).

In terms of simulation in Figure 11 a), the amplitude of the waveform was lower from pit and SMP low resolution (5 cm) measurements compared with the micro-CT and SMP high-resolution (1 cm). The SMRT simulations with different sources of snow measurement inputs, but of the same resolution (1 and 5 cm), produced similar simulation results. In Figure 11 b), all pit (AK1-AK4) amplitudes were smaller than micro-CT amplitudes. The difference between simulations was driven by the snow density since the snow depth was similar and temperature and salinity were the same for pits, SMP and micro-CT simulations and as shown earlier, microstructure may not contribute to the amplitude of the waveform at Ku-band (Figure 6).

https://doi.org/10.5194/egusphere-2026-3615
Preprint. Discussion started: 13 July 2026

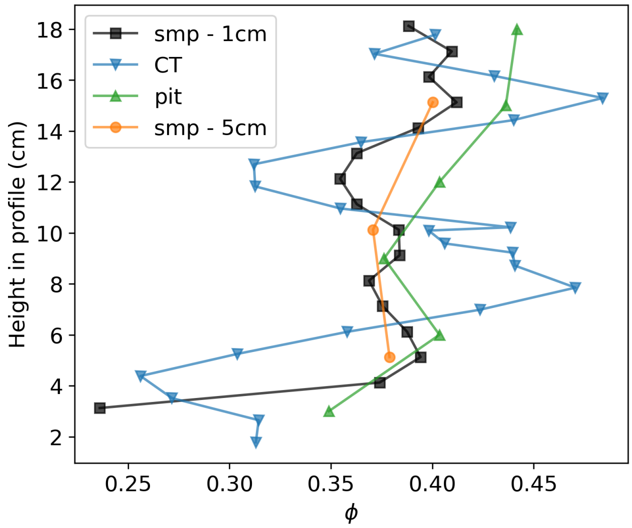

Figure 10. Comparison of volume fraction between snowpit measurements (density cutter), SMP and micro-CT measurements for CB-22.

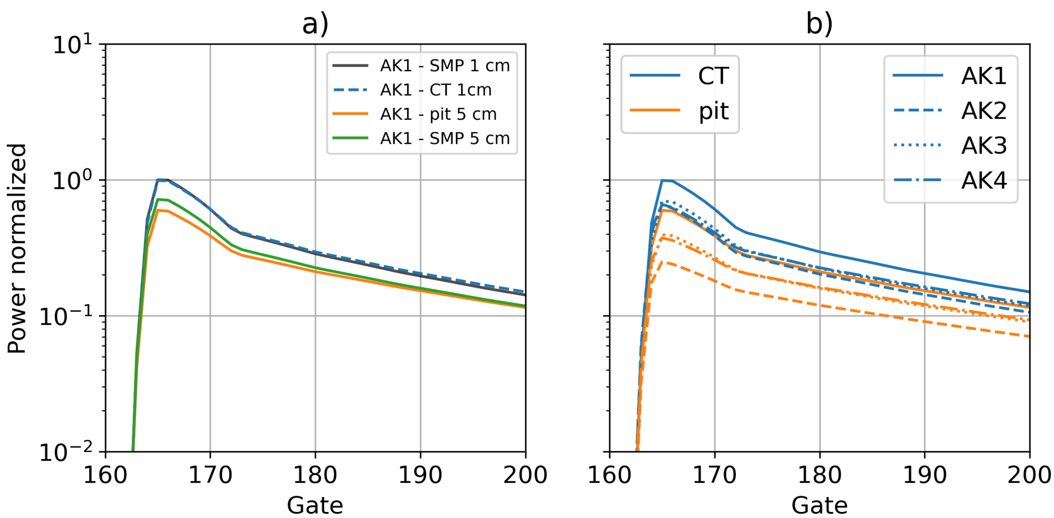

Figure 11. Comparison of SMRT simulation between instruments and processed data resolutions, a) simulations between SMP (1 cm), micro-CT (1 cm), pit (5 cm) and SMP (5 cm). b) differences in simulations between pit and micro-CT at four sites in CB-22.

4 Discussion

SMRT can successfully simulate waveforms of altimeters on sea ice provided appropriate radar-scale roughness parameters are used. Figure 4 indicates that simulations of smooth FYI must incorporate coherent reflections as reported by De Rijke-Thomas et al. (2023), whereas MYI mostly needs incoherent returns. Accurately modelling the amplitude, the interplay between co-

https://doi.org/10.5194/egusphere-2026-3615
Preprint. Discussion started: 13 July 2026

herent and incoherent returns, and the signal's waveform decay for various sea ice types (FYI and MYI) requires site-specific, optimized surface roughness parameters. The roughness is the only parameter affecting both the peakiness (coherent return) and the decay (other than mispointing). This allows us to estimate the radar-scale roughness (s and l) from the observed waveform which is critical for sea ice thickness retrieval (Landy et al., 2020).

Using the IEM surface scattering domain assumption, optimized roughness values (Table 3) were found to be similar to previously reported measured values in the literature (Landy et al., 2015). The measured roughness for flat ice in CB-22 and Eureka-22 (Table 2, s_{ice} = 1.5mm) is lower than the optimized values in CB-22 (s_{ice} = 2.9 mm) and Eureka-22 (s_{ice} = 3.0 mm). This may be due to our in-situ measurement method, which could artificially flatten the ice surface when removing the snow with a shovel. This remains a challenging field observation to make. Values optimized for all sites were consistent with values measured from Table 3 in Landy et al. (2015). For Alert-17 and Eureka-16, a rougher sea ice resulted in the incoherent return dominating. The optimized snow roughness was similar for all sites and similar to the measured roughness. This indicates the snow roughness is not a function of ice type. For l, the optimized values for all sites were much higher than the measured values (l_{ice} = 5.2 cm) and reached the maximum of the optimized range for CB-22 and Eureka-22. Those higher values were needed to correctly simulate the waveform. A larger correlation length should represent a smoother surface, but our measured values for flat ice were smaller than rough sea ice and snow which might indicate a potential problem in the in-situ roughness measurement method for l. The areas investigated were potentially not large enough (horizontally) to estimate the correct length. Estimated values (s and l) are dependent on the detrending method, and a community consensus on which method to estimate roughness relevant to microwave radiative transfer is still lacking. This study confirms this difficulty. Overall, the optimized roughness parametrization gave an appropriate fit with the Ku-band waveform, but it is still unclear if the roughness values are realistic. The optimization and measurements of roughness are not trivial and remain the most challenging parameter to quantify in models of sea ice altimetry.

SMRT simulations showed that the radar echoes at Ku-band came from the reflection at the snow and sea ice surface, with relative contributions depending on the radar-scale roughness. Waveform amplitudes were sensitive to snow parameters that changed the effective permittivity and therefore, interface reflectivity. Sea ice parameters were also found to influence the reflection to a lesser extent as they modify the permittivity of the ice surface. It can be concluded that the altimeter signal at Ku-band is sensitive to changes in the effective permittivity of the snowpack and the ice. Note that snow density also affects the speed of the wave and in turn the estimated surface elevation, which has not been investigated here. The low sensitivity to snow microstructure is likely due to the strict nadir angle used in the simulations. This behavior is different for SAR imagery with a higher incidence angle, which leads to a stronger component of volume scattering at Ku-band (King et al., 2018). This suggests that a model similar to Landy et al. (2019) that simplifies volume scattering from microstructure, but incorporates complex roughness interactions (at two scales) could be sufficient to model Ku-band altimeter observations.

Snow properties have an impact on the track-point by modifying the amplitude of the radar echoes for both frequencies as was shown in Figures 6 and 7. An appropriate radiative transfer model of snow will be needed to correctly infer snow depth from track-point differences at Ku- and Ka-band since this study showed how sensitive both frequencies were to snow parameters. Of all snow parameters, snow density showed the strongest influence on the amplitude of Ku- and Ka-band. This

https://doi.org/10.5194/egusphere-2026-3615
Preprint. Discussion started: 13 July 2026

sensitivity also opens the opportunity to improve retrieval of snow depth like inFons et al. (2023). This has implications for sea ice thickness retrieval because uncertainty in snow density estimates can lead to bias up to 30 cm in ice thickness estimation (Kern et al., 2015).

The high-resolution micro-CT snow measurements were evaluated in SMRT simulations and produced consistently higher amplitudes for all CB-22 sites compared to low-resolution pit and SMP. This is likely due to the enhanced vertical information in snow density (Figure 10) provided by the micro-CT measurement and SMP at high-resolution. Figure 10 showed large changes in volume fraction from the CT compared to a steady decrease in density from the pit and SMP low resolution. These substantial changes in density increased reflection from interfaces between snow layers. However, the layer thicknesses can not be smaller than the wavelength in SMRT so 1 cm is on the limit for Ku-band. Nonetheless, using a 1-layer model with bulk density might underestimate the reflection of the altimeter signal, and the non-uniform structure of the snowpack should be included in a full error budget analysis for future radar altimeter retrieval algorithms.

Knowledge of sea ice roughness is critical to ascertain whether the radar signal is predominantly from the snow surface, ice surface, or volume scattering in the snow. When roughness was optimized (Table 3), the Ku-band signal came mostly from the snow surface for MYI and from the ice surface for FYI for these sites. For Ka-band, the signal came mostly from the snow surface. Questions still arise on which model (IEM or GO) should be used at Ka (Figure 8). The roughness set for Ka-band resulted from an optimization at Ku-band and is also on the limit of the IEM model (ks < 3). This highlights the importance of the roughness parameters in SMRT for altimeter applications.

The microstructure of snow had a noticeable but small effect on the simulated total power at Ka-band. The altimeter signal at Ka-band is affected by the snow density like Ku-band, but was also sensitive to the microstructure of snow. Figure 9 c) showed a 10% drop in power contribution for 40% sensitive to SSA. Volume scattering by SMRT altimeter is underestimated at higher frequency (Ka-band) since it is a first order scattering model. Implementing higher order for multiple scattering within the snowpack and the improved IEM (IIEM) to account for multiple scattering of the ice surface should be considered going forward (Larue et al., 2021).

The domination of the snow surface signal contribution for both Ku and Ka-band on MYI is consistent with the findings from (Willatt et al., 2023), which found that the highest amplitude peak of a ground-based Radar at the Ku and Ka-band was closer to the snow surface than the ice on second-year ice. Similar findings were also reported in Antarctica Willatt et al. (2025); Fredensborg Hansen et al. (2025). For smoother ice, the coherent reflection from the quasi-specular ice surfaces (De Rijke-Thomas et al., 2023) becomes stronger than the snow surface so that the scattering horizon at Ku-band represents the ice surface. Knowledge of what the waveform track-point represents is crucial if we want to retrieve snow depth from the difference between Ka- and Ku-band track-points (Lawrence et al., 2018). Our findings suggest that retrieving snow depth from Ka and Ku may be possible for smooth FYI but less effective for rough MYI. However, further investigation is needed since there are several parameters that can affect the scattering surface (e.g., roughness and snow properties) and thus the behavior of the scattering horizon.

Future developments of SMRT for sea ice altimetry could help mitigate issues and improve the simulations to help to better constrain the roughness and determine the respective contributions of the surfaces. Some developments include a waveform

https://doi.org/10.5194/egusphere-2026-3615
Preprint. Discussion started: 13 July 2026

model for SAR mode (Picard et al., 2026), a 3-phase medium (ice, air and brine) and adding multiple scattering for Ka-band and big grains. A log-normal probability distribution (Landy et al., 2020) function may be more representative over snow-covered sea ice and can not be implemented in the current LRM implementation in SMRT. However, it is available for SAR mode (Picard et al., 2026) using numerical facets modelling.

5 Conclusion

In this paper, we demonstrated the capabilities and limitations of SMRT to simulate altimetric waveforms over sea ice for three different regions with distinct ice types and snow cover over multiple seasons, with good fit to CryoSat2 observations. This includes the ability to demonstrate the proportion of signal coming from the snow surface, sea ice surface and snow volume scattering, which was not done before. SMRT showed that snow and sea ice properties had a notable impact on the reflected signal (amplitude). The most critical parameter in SMRT simulation is the roughness of the sea ice since it dictates how much power is reflected at the ice surface, which could be challenging for physical retrackers. Through identification of the main scattering horizons, we showed that for FYI (Figure 8) the signal comes mostly from the ice surface at Ku-band and from the snow surface at Ka-band, which is encouraging for snow depth retrieval and the CRISTAL mission. However, our results also suggest this would be challenging for rougher ice because the signal predominantly comes from the snow surface at both frequencies. Considering snow properties with a physical retracker will be necessary since snow properties shift the track-point for both frequencies (Figure 6 and 7). SMRT could improve the retrieval of snow depth, snow density and ice thickness using the model as a base for a physical retracker for the CRISTAL mission. This study improved our understanding of the interaction between the radar altimeter signal and sea ice by using a radiative transfer approach based on state-of-the-art in-situ snow measurements.

Code and data availability. Code for this paper are available at https://github.com/JulienMeloche/AKROSS_paper.
SMRT release version: https://github.com/smrt-model/smrt/releases/tag/v1.5.1
Data from CB-22 (AKROSS) is available at DOI: 10.5281/zenodo.11205157.
Data from Eureka-22 is available at (to be added).
Data from Alert-17 and Eureka-16 is available at DOI: 10.5281/zenodo.4068349.

https://doi.org/10.5194/egusphere-2026-3615
Preprint. Discussion started: 13 July 2026

Appendix A: List of Symbols

L	mean distance between structural elements in 3D
$\tilde{F}$	median of the penetration resistance force
d_i	SMP specific surface area coefficients
Δt	time
$P_\mathrm{r}(t)$	Returned power at the Radar
$P_\mathrm{t}(t)$	Transmitted power of the Radar
$pdf(t)$	probability density function of the surface
$P_\mathrm{FS}(t)$	Flat surface impulse
σ^0_s	backscattering coefficient of the surface
σ^0_int	backscattering coefficient of the interface
$\delta(t)$	dirac delta function
I_int	specific intensities from interface reflection
I_vol	specific intensities from volume scattering
mss	mean square slope
s	radar-scale rms height of the ice or snow surface (s_ice or s_snow)
l	radar-scale correlation length of the ice or snow surface (l_ice or l_snow)
σ_surf	large scale rms height of the surface
G_0	peak antenna gain at boresight
h	height of satellite
λ	wavelength of the sensor
β	beamwidth of the sensor
θ	incident angle
c	speed of light
R	radius of the Earth
I_0	first component of the Bessel function
l_mw	microwave microstructural lenght
l_p	porod length
ρ_s	density of snow
ρ_i	density of ice
κ	polydispersity of snow
Λ	normalisation factor
A_i	Amplitude of the waveform i

https://doi.org/10.5194/egusphere-2026-3615
Preprint. Discussion started: 13 July 2026

Appendix B: roughness

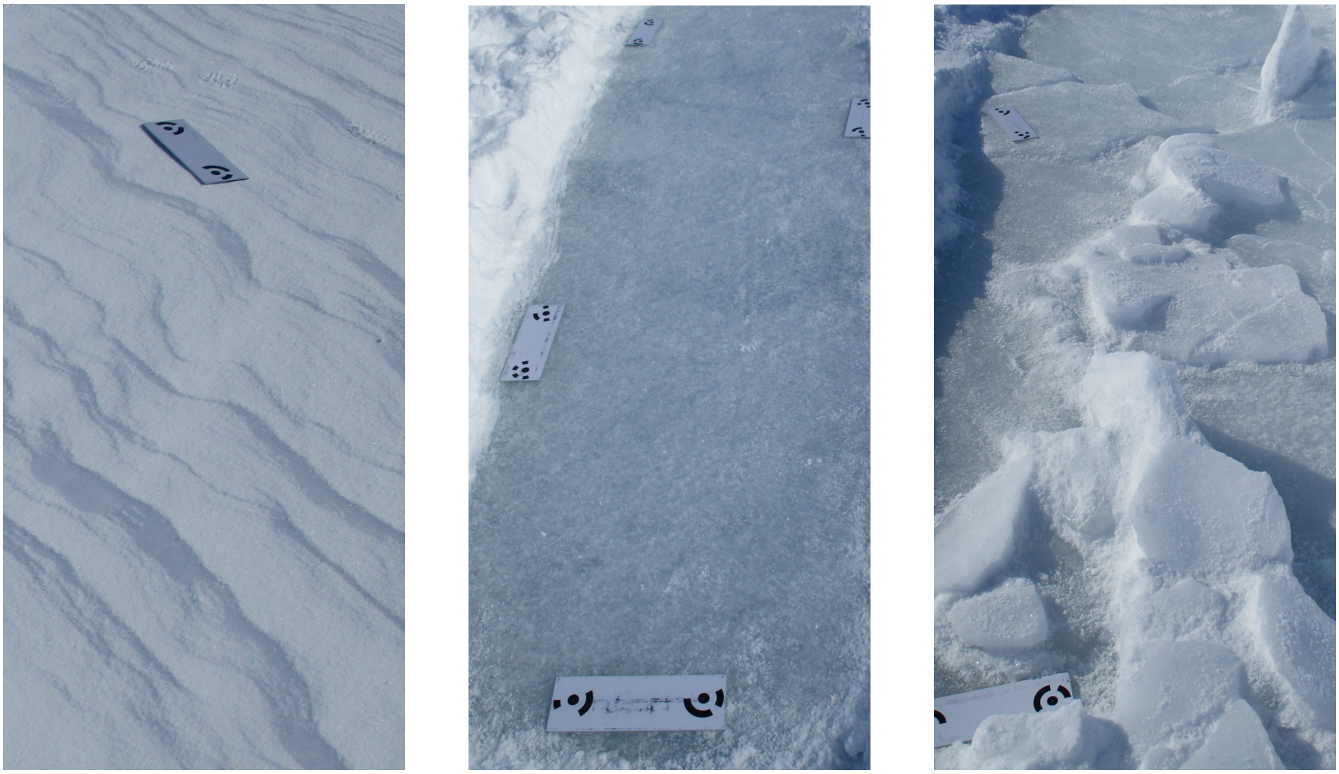

(a) (b) (c)

Figure B1. a) Snow surface (n = 11), b) flat sea ice (n = 9) and c) rough sea ice (n =3)

Appendix C: Salinity Measurements

Table C1. Overview of ice thickness and salinity measurements from the different sites.

		Salinity (PSU)		
Site	Ice thickness (m)	Ice surface	Snow base layers (<= 6 cm)	Snow top layers (> 6 cm)
Eureka-16	1.80	4.2	3.6	0.3
Alert-17	2.17	2.0	2.0	0.1
CB-22	1.84	9.3	7.9	1.0
Eureka-22	1.96	16.8	11.9	1.0

https://doi.org/10.5194/egusphere-2026-3615
Preprint. Discussion started: 13 July 2026

Appendix D: Waveform alignment

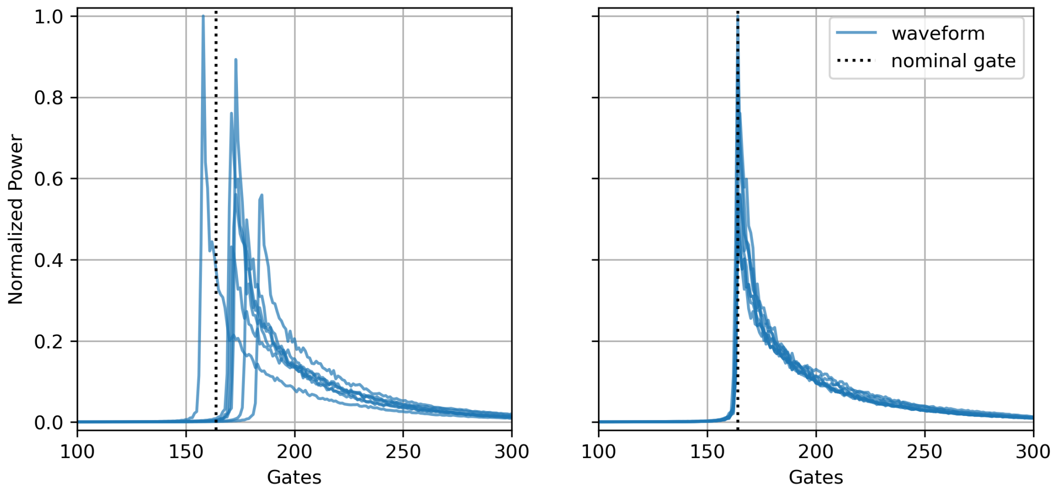

Figure D1. Alignment of observed waveform to the nominal gate (164).

Author contributions. JM wrote the manuscript with contributions from all co-authors. MS, HL and NR designed the experiment. JM, MS, HL and GP performed the analysis. JM, MS, HL, NR, RE, RS, PT, JK, AL and CH collected the field measurements. MJ and HL analysed and developed the Micro-CT data and protocol. GP wrote the code of the model used. JB, AB and MS provided guidance with the CryoSat-2 data. All co-authors reviewed the manuscript and provided analysis guidance.

Competing interests. Some authors are members of the editorial board of The Cryosphere.

Acknowledgements. We wish to respectfully acknowledge the late Dr. Henning Löwe and Dr. Josh King for their outstanding contributions to the field of snow science. Their expertise, passion, and dedication had a profound impact on both the discipline and our community. As esteemed colleagues and cherished friends, they are deeply missed, and their legacy will continue to inspire us.

This work was funded under the ESA AKROSS project, ESA CONTRACT NO. 4000130073/20/I-DT and was only possible thanks to extensive logistical the Canadian High Arctic Research Station (particularly Martin Leger) and Polar Knowledge Canada. The authors would also like to thank Adrià Blanco (University of Victoria), John Yackel, Hoi Ming Lam and Monojit Saha (University of Calgary), and the whole GRIMP team from Sherbrooke in particular Charlotte Crevier and Caroline Dolant for the shipping of dangerous goods and Juliette Ortet for her tea etiquette.

https://doi.org/10.5194/egusphere-2026-3615
Preprint. Discussion started: 13 July 2026

References

Allard, R. A., Farrell, S. L., Hebert, D. A., Johnston, W. F., Li, L., Kurtz, N. T., Phelps, M. W., Posey, P. G., Tilling, R., Ridout, A., and Wallcraft, A. J.: Utilizing CryoSat-2 Sea Ice Thickness to Initialize a Coupled Ice-Ocean Modeling System, Advances in Space Research, 62, 1265–1280, https://doi.org/10.1016/j.asr.2017.12.030, 2018.

Blockley, E. W. and Peterson, K. A.: Improving Met Office Seasonal Predictions of Arctic Sea Ice Using Assimilation of CryoSat-2 Thickness, The Cryosphere, 12, 3419–3438, https://doi.org/10.5194/tc-12-3419-2018, 2018.

Brown, G.: The Average Impulse Response of a Rough Surface and Its Applications, IEEE Transactions on Antennas and Propagation, 25, 67–74, https://doi.org/10.1109/TAP.1977.1141536, 1977.

De Rijke-Thomas, C., Landy, J. C., Mallett, R., Willatt, R. C., Tsamados, M., and King, J.: Airborne Investigation of Quasi-Specular Ku-Band Radar Scattering for Satellite Altimetry Over Snow-Covered Arctic Sea Ice, IEEE Transactions on Geoscience and Remote Sensing, 61, 1–19, https://doi.org/10.1109/TGRS.2023.3318263, 2023.

Dinardo, S., Fenoglio-Marc, L., Buchhaupt, C., Becker, M., Scharroo, R., Joana Fernandes, M., and Benveniste, J.: Coastal SAR and PLRM Altimetry in German Bight and West Baltic Sea, Advances in Space Research, 62, 1371–1404, https://doi.org/10.1016/j.asr.2017.12.018, 2018.

Fan, Y., Li, L., Chen, H., and Guan, L.: Evaluation and Application of SMRT Model for L-Band Brightness Temperature Simulation in Arctic Sea Ice, Remote Sensing, 15, 3889, https://doi.org/10.3390/rs15153889, 2023.

Ferraro, E. J. and Swift, C. T.: Measuring Geophysical Parameters of the Greenland Ice Sheet Using Airborne Radar Altimetry, Journal of Glaciology, 41, 607–618, https://doi.org/10.3189/S0022143000034924, 1995.

Fons, S., Kurtz, N., and Bagnardi, M.: A Decade-plus of Antarctic Sea Ice Thickness and Volume Estimates from CryoSat-2 Using a Physical Model and Waveform Fitting, The Cryosphere, 17, 2487–2508, https://doi.org/10.5194/tc-17-2487-2023, 2023.

Fons, S. W. and Kurtz, N. T.: Retrieval of Snow Freeboard of Antarctic Sea Ice Using Waveform Fitting of CryoSat-2 Returns, The Cryosphere, 13, 861–878, https://doi.org/10.5194/tc-13-861-2019, 2019.

Fredensborg Hansen, R. M., Rinne, E., and Skourup, H.: Classification of Sea Ice Types in the Arctic by Radar Echoes from SARAL/AltiKa, Remote Sensing, 13, 3183, https://doi.org/10.3390/rs13163183, 2021.

Fredensborg Hansen, R. M., Skourup, H., Rinne, E., Jutila, A., Lawrence, I. R., Shepherd, A., Høyland, K. V., Li, J., Rodriguez-Morales, F., Simonsen, S. B., Wilkinson, J., Veyssiere, G., Yi, D., Forsberg, R., and Casal, T. G. D.: Multi-Frequency Altimetry Snow Depth Estimates over Heterogeneous Snow-Covered Antarctic Summer Sea Ice – Part 1: C/S-, Ku-, and Ka-band Airborne Observations, The Cryosphere, 19, 4167–4192, https://doi.org/10.5194/tc-19-4167-2025, 2025.

Geldsetzer, T., Langlois, A., and Yackel, J.: Dielectric Properties of Brine-Wetted Snow on First-Year Sea Ice, Cold Regions Science and Technology, 58, 47–56, https://doi.org/10.1016/j.coldregions.2009.03.009, 2009.

Goosse, H., Kay, J. E., Armour, K. C., Bodas-Salcedo, A., Chepfer, H., Docquier, D., Jonko, A., Kushner, P. J., Lecomte, O., Massonnet, F., Park, H.-S., Pithan, F., Svensson, G., and Vancoppenolle, M.: Quantifying Climate Feedbacks in Polar Regions, Nature Communications, 9, 1919, https://doi.org/10.1038/s41467-018-04173-0, 2018.

Guerreiro, K., Fleury, S., Zakharova, E., Rémy, F., and Kouraev, A.: Potential for Estimation of Snow Depth on Arctic Sea Ice from CryoSat-2 and SARAL/AltiKa Missions, Remote Sensing of Environment, 186, 339–349, https://doi.org/10.1016/j.rse.2016.07.013, 2016.

Haas, C., Beckers, J., King, J., Silis, A., Stroeve, J., Wilkinson, J., Notenboom, B., Schweiger, A., and Hendricks, S.: Ice and Snow Thickness Variability and Change in the High Arctic Ocean Observed by In Situ Measurements: Arctic Sea Ice and Snow Thickness, Geophysical Research Letters, 44, 10,462–10,469, https://doi.org/10.1002/2017GL075434, 2017.

Hayne, G.: Radar Altimeter Mean Return Waveforms from Near-Normal-Incidence Ocean Surface Scattering, IEEE Transactions on Antennas and Propagation, 28, 687–692, https://doi.org/10.1109/TAP.1980.1142398, 1980.

Kern, M., Cullen, R., Berruti, B., Bouffard, J., Casal, T., Drinkwater, M. R., Gabriele, A., Lecuyot, A., Ludwig, M., Midthassel, R., Navas Traver, I., Parrinello, T., Ressler, G., Andersson, E., Martin-Puig, C., Andersen, O., Bartsch, A., Farrell, S., Fleury, S., Gascoin, S., Guillot, A., Humbert, A., Rinne, E., Shepherd, A., Van Den Broeke, M. R., and Yackel, J.: The Copernicus Polar Ice and Snow Topography Altimeter (CRISTAL) High-Priority Candidate Mission, The Cryosphere, 14, 2235–2251, https://doi.org/10.5194/tc-14-2235-2020, 2020.

Kern, S., Khvorostovsky, K., Skourup, H., Rinne, E., Parsakhoo, Z. S., Djepa, V., Wadhams, P., and Sandven, S.: The Impact of Snow Depth, Snow Density and Ice Density on Sea Ice Thickness Retrieval from Satellite Radar Altimetry: Results from the ESA-CCI Sea Ice ECV Project Round Robin Exercise, The Cryosphere, 9, 37–52, https://doi.org/10.5194/tc-9-37-2015, 2015.

King, J., Derksen, C., Toose, P., Langlois, A., Larsen, C., Lemmetyinen, J., Marsh, P., Montpetit, B., Roy, A., Rutter, N., and Sturm, M.: The Influence of Snow Microstructure on Dual-Frequency Radar Measurements in a Tundra Environment, Remote Sensing of Environment, 215, 242–254, https://doi.org/10.1016/j.rse.2018.05.028, 2018.

King, J., Howell, S., Brady, M., Toose, P., Derksen, C., Haas, C., and Beckers, J.: Local-Scale Variability of Snow Density on Arctic Sea Ice, The Cryosphere, 14, 4323–4339, https://doi.org/10.5194/tc-14-4323-2020, 2020.

Kurtz, N. T., Galin, N., and Studinger, M.: An Improved CryoSat-2 Sea Ice Freeboard Retrieval Algorithm through the Use of Waveform Fitting, The Cryosphere, 8, 1217–1237, https://doi.org/10.5194/tc-8-1217-2014, 2014.

Kwok, R.: Simulated Effects of a Snow Layer on Retrieval of CryoSat-2 Sea Ice Freeboard, Geophysical Research Letters, 41, 5014–5020, https://doi.org/10.1002/2014GL060993, 2014.

Landy, J. C., Isleifson, D., Komarov, A. S., and Barber, D. G.: Parameterization of Centimeter-Scale Sea Ice Surface Roughness Using Terrestrial LiDAR, IEEE Transactions on Geoscience and Remote Sensing, 53, 1271–1286, https://doi.org/10.1109/TGRS.2014.2336833, 2015.

Landy, J. C., Tsamados, M., and Scharien, R. K.: A Facet-Based Numerical Model for Simulating SAR Altimeter Echoes From Heterogeneous Sea Ice Surfaces, IEEE Transactions on Geoscience and Remote Sensing, 57, 4164–4180, https://doi.org/10.1109/TGRS.2018.2889763, 2019.

Landy, J. C., Petty, A. A., Tsamados, M., and Stroeve, J. C.: Sea Ice Roughness Overlooked as a Key Source of Uncertainty in CryoSat-2 Ice Freeboard Retrievals, Journal of Geophysical Research: Oceans, 125, e2019JC015 820, https://doi.org/10.1029/2019JC015820, 2020.

Landy, J. C., De Rijke-Thomas, C., Nab, C., Lawrence, I., Glissenaar, I. A., Mallett, R. D. C., Fredensborg Hansen, R. M., Petty, A., Tsamados, M., Macfarlane, A. R., and Braakmann-Folgmann, A.: Anticipating CRISTAL: An Exploration of Multi-Frequency Satellite Altimeter Snow Depth Estimates over Arctic Sea Ice, 2018–2023, The Cryosphere, 20, 183–208, https://doi.org/10.5194/tc-20-183-2026, 2026.

Larue, F., Picard, G., Aublanc, J., Arnaud, L., Robledano-Perez, A., LE Meur, E., Favier, V., Jourdain, B., Savarino, J., and Thibaut, P.: Radar Altimeter Waveform Simulations in Antarctica with the Snow Microwave Radiative Transfer Model (SMRT), Remote Sensing of Environment, 263, 112 534, https://doi.org/10.1016/j.rse.2021.112534, 2021.

Lawrence, I. R., Tsamados, M. C., Stroeve, J. C., Armitage, T. W. K., and Ridout, A. L.: Estimating Snow Depth over Arctic Sea Ice from Calibrated Dual-Frequency Radar Freeboards, The Cryosphere, 12, 3551–3564, https://doi.org/10.5194/tc-12-3551-2018, 2018.

Laxon, S. W., Giles, K. A., Ridout, A. L., Wingham, D. J., Willatt, R., Cullen, R., Kwok, R., Schweiger, A., Zhang, J., Haas, C., Hendricks, S., Krishfield, R., Kurtz, N., Farrell, S., and Davidson, M.: CryoSat-2 Estimates of Arctic Sea Ice Thickness and Volume: CRYOSAT-2 SEA ICE THICKNESS AND VOLUME, Geophysical Research Letters, 40, 732–737, https://doi.org/10.1002/grl.50193, 2013.

Legresy, B., Papa, F., Remy, F., Vinay, G., van den Bosch, M., and Zanife, O.-Z.: ENVISAT Radar Altimeter Measurements over Continental Surfaces and Ice Caps Using the ICE-2 Retracking Algorithm, Remote Sensing of Environment, 95, 150–163, https://doi.org/10.1016/j.rse.2004.11.018, 2005.

Löwe, H. and van Herwijnen, A.: A Poisson Shot Noise Model for Micro-Penetration of Snow, Cold Regions Science and Technology, 70, 62–70, https://doi.org/10.1016/j.coldregions.2011.09.001, 2012.

Meloche, J., Royer, A., Langlois, A., Rutter, N., and Sasseville, V.: Improvement of Microwave Emissivity Parameterization of Frozen Arctic Soils Using Roughness Measurements Derived from Photogrammetry, International Journal of Digital Earth, 14, 1380–1396, https://doi.org/10.1080/17538947.2020.1836049, 2021.

Montpetit, B., King, J., Meloche, J., Derksen, C., Siqueira, P., Adam, J. M., Toose, P., Brady, M., Wendleder, A., Vionnet, V., and Leroux, N. R.: Retrieval of Snow and Soil Properties for Forward Radiative Transfer Modeling of Airborne Ku-band SAR to Estimate Snow Water Equivalent: The Trail Valley Creek 2018/19 Snow Experiment, The Cryosphere, 18, 3857–3874, https://doi.org/10.5194/tc-18-3857-2024, 2024.

Mudryk, L. R., Derksen, C., Howell, S., Laliberté, F., Thackeray, C., Sospedra-Alfonso, R., Vionnet, V., Kushner, P. J., and Brown, R.: Canadian Snow and Sea Ice: Historical Trends and Projections, The Cryosphere, 12, 1157–1176, https://doi.org/10.5194/tc-12-1157-2018, 2018.

Murfitt, J., Duguay, C. R., Picard, G., and Gunn, G. E.: Investigating the Effect of Lake Ice Properties on Multifrequency Backscatter Using the Snow Microwave Radiative Transfer Model, IEEE Transactions on Geoscience and Remote Sensing, 60, 1–23, https://doi.org/10.1109/TGRS.2022.3197109, 2022.

Murfitt, J., Duguay, C., Picard, G., and Gunn, G.: Forward Modelling of Synthetic Aperture Radar Backscatter from Lake Ice over Canadian Subarctic Lakes, Remote Sensing of Environment, 286, 113 424, https://doi.org/10.1016/j.rse.2022.113424, 2023.

Nandan, V., Geldsetzer, T., Yackel, J., Mahmud, M., Scharien, R., Howell, S., King, J., Ricker, R., and Else, B.: Effect of Snow Salinity on CryoSat-2 Arctic First-Year Sea Ice Freeboard Measurements: Sea Ice Brine-Snow Effect on CryoSat-2, Geophysical Research Letters, 44, 10,419–10,426, https://doi.org/10.1002/2017GL074506, 2017.

Nandan, V., Scharien, R. K., Geldsetzer, T., Kwok, R., Yackel, J. J., Mahmud, M. S., Rosel, A., Tonboe, R., Granskog, M., Willatt, R., Stroeve, J., Nomura, D., and Frey, M.: Snow Property Controls on Modeled Ku-Band Altimeter Estimates of First-Year Sea Ice Thickness: Case Studies From the Canadian and Norwegian Arctic, IEEE Journal of Selected Topics in Applied Earth Observations and Remote Sensing, 13, 1082–1096, https://doi.org/10.1109/JSTARS.2020.2966432, 2020.

Nicolaus, M., Perovich, D. K., Spreen, G., Granskog, M. A., Von Albedyll, L., Angelopoulos, M., Anhaus, P., Arndt, S., Belter, H. J., Bessonov, V., Birnbaum, G., Brauchle, J., Calmer, R., Cardellach, E., Cheng, B., Clemens-Sewall, D., Dadic, R., Damm, E., De Boer, G., Demir, O., Dethloff, K., Divine, D. V., Fong, A. A., Fons, S., Frey, M. M., Fuchs, N., Gabarró, C., Gerland, S., Goessling, H. F., Gradinger, R., Haapala, J., Haas, C., Hamilton, J., Hannula, H.-R., Hendricks, S., Herber, A., Heuzé, C., Hoppmann, M., Høyland, K. V., Huntemann, M., Hutchings, J. K., Hwang, B., Itkin, P., Jacobi, H.-W., Jaggi, M., Jutila, A., Kaleschke, L., Katlein, C., Kolabutin, N., Krampe, D., Kristensen, S. S., Krumpen, T., Kurtz, N., Lampert, A., Lange, B. A., Lei, R., Light, B., Linhardt, F., Liston, G. E., Loose, B., Macfarlane, A. R., Mahmud, M., Matero, I. O., Maus, S., Morgenstern, A., Naderpour, R., Nandan, V., Niubom, A., Oggier, M., Oppelt, N., Pätzold, F., Perron, C., Petrovsky, T., Pirazzini, R., Polashenski, C., Rabe, B., Raphael, I. A., Regnery, J., Rex, M., Ricker, R., Riemann-Campe, K., Rinke, A., Rohde, J., Salganik, E., Scharien, R. K., Schiller, M., Schneebeli, M., Semmling, M., Shimanchuk, E., Shupe, M. D., Smith, M. M., Smolyanitsky, V., Sokolov, V., Stanton, T., Stroeve, J., Thielke, L., Timofeeva, A., Tonboe, R. T., Tavri, A., Tsamados, M., Wagner, D. N., Watkins, D., Webster, M., and Wendisch, M.: Overview of the MOSAiC Expedition: Snow and Sea Ice, Elementa: Science of the Anthropocene, 10, 000 046, https://doi.org/10.1525/elementa.2021.000046, 2022.

Picard, G., Sandells, M., and Löwe, H.: SMRT: An Active–Passive Microwave Radiative Transfer Model for Snow with Multiple Microstructure and Scattering Formulations (v1.0), Geoscientific Model Development, 11, 2763–2788, https://doi.org/10.5194/gmd-11-2763-2018, 2018.

Picard, G., Löwe, H., Domine, F., Arnaud, L., Larue, F., Favier, V., Le Meur, E., Lefebvre, E., Savarino, J., and Royer, A.: The Microwave Snow Grain Size: A New Concept to Predict Satellite Observations Over Snow-Covered Regions, AGU Advances, 3, https://doi.org/10.1029/2021AV000630, 2022.

Picard, G., Murfitt, J., Zakharova, E., Zeiger, P., Arnaud, L., Aublanc, J., Landy, J. C., Scagliola, M., and Duguay, C.: Simulating SAR Altimeter Echoes from Cryospheric Surfaces with the Snow Microwave Radiative Transfer (SMRT) Model Version Sarm-V0, https://doi.org/10.5194/egusphere-2025-6056, 2026.

Proksch, M., Rutter, N., Fierz, C., and Schneebeli, M.: Intercomparison of Snow Density Measurements: Bias, Precision, and Vertical Resolution, The Cryosphere, 10, 371–384, https://doi.org/10.5194/tc-10-371-2016, 2016.

Quartly, G. D., Rinne, E., Passaro, M., Andersen, O. B., Dinardo, S., Fleury, S., Guillot, A., Hendricks, S., Kurekin, A. A., Müller, F. L., Ricker, R., Skourup, H., and Tsamados, M.: Retrieving Sea Level and Freeboard in the Arctic: A Review of Current Radar Altimetry Methodologies and Future Perspectives, Remote Sensing, 11, 881, https://doi.org/10.3390/rs11070881, 2019.

Richter-Menge, J., J. E. Overland, J. T. Mathis, and E. Osborne: Arctic Report Card 2017, 2017.

Ricker, R., Hendricks, S., Helm, V., Skourup, H., and Davidson, M.: Sensitivity of CryoSat-2 Arctic Sea-Ice Freeboard and Thickness on Radar-Waveform Interpretation, The Cryosphere, 8, 1607–1622, https://doi.org/10.5194/tc-8-1607-2014, 2014.

Ricker, R., Hendricks, S., and Beckers, J.: The Impact of Geophysical Corrections on Sea-Ice Freeboard Retrieved from Satellite Altimetry, Remote Sensing, 8, 317, https://doi.org/10.3390/rs8040317, 2016.

Sandells, M., Lowe, H., Picard, G., Dumont, M., Essery, R., Floury, N., Kontu, A., Lemmetyinen, J., Maslanka, W., Morin, S., Wiesmann, A., and Matzler, C.: X-Ray Tomography-Based Microstructure Representation in the Snow Microwave Radiative Transfer Model, IEEE Transactions on Geoscience and Remote Sensing, 60, 1–15, https://doi.org/10.1109/TGRS.2021.3086412, 2022.

Serreze, M. C. and Barry, R. G.: Processes and Impacts of Arctic Amplification: A Research Synthesis, Global and Planetary Change, 77, 85–96, https://doi.org/10.1016/j.gloplacha.2011.03.004, 2011.

Serreze, M. C. and Meier, W. N.: The Arctic's Sea Ice Cover: Trends, Variability, Predictability, and Comparisons to the Antarctic, Annals of the New York Academy of Sciences, 1436, 36–53, https://doi.org/10.1111/nyas.13856, 2019.

Soriot, C., Picard, G., Prigent, C., Frappart, F., and Domine, F.: Year-Round Sea Ice and Snow Characterization from Combined Passive and Active Microwave Observations and Radiative Transfer Modeling, Remote Sensing of Environment, 278, 113 061, https://doi.org/10.1016/j.rse.2022.113061, 2022.

Tsang, L., Pan, J., Liang, D., Li, Z., Cline, D. W., and Tan, Y.: Modeling Active Microwave Remote Sensing of Snow Using Dense Media Radiative Transfer (DMRT) Theory With Multiple-Scattering Effects, IEEE Transactions on Geoscience and Remote Sensing, 45, 990–1004, https://doi.org/10.1109/TGRS.2006.888854, 2007.

Tsang, L., Durand, M., Derksen, C., Barros, A. P., Kang, D.-H., Lievens, H., Marshall, H.-P., Zhu, J., Johnson, J., King, J., Lemmetyinen, J., Sandells, M., Rutter, N., Siqueira, P., Nolin, A., Osmanoglu, B., Vuyovich, C., Kim, E., Taylor, D., Merkouriadi, I., Brucker, L., Navari,

https://doi.org/10.5194/egusphere-2026-3615
Preprint. Discussion started: 13 July 2026

M., Dumont, M., Kelly, R., Kim, R. S., Liao, T.-H., Borah, F., and Xu, X.: Review Article: Global Monitoring of Snow Water Equivalent Using High-Frequency Radar Remote Sensing, The Cryosphere, 16, 3531–3573, https://doi.org/10.5194/tc-16-3531-2022, 2022.

Vargel, C., Royer, A., St-Jean-Rondeau, O., Picard, G., Roy, A., Sasseville, V., and Langlois, A.: Arctic and Subarctic Snow Microstructure Analysis for Microwave Brightness Temperature Simulations, Remote Sensing of Environment, 242, 111 754, https://doi.org/10.1016/j.rse.2020.111754, 2020.

Willatt, R., Stroeve, J. C., Nandan, V., Newman, T., Mallett, R., Hendricks, S., Ricker, R., Mead, J., Itkin, P., Tonboe, R., Wagner, D. N., Spreen, G., Liston, G., Schneebeli, M., Krampe, D., Tsamados, M., Demir, O., Wilkinson, J., Jaggi, M., Zhou, L., Huntemann, M., Raphael, I. A., Jutila, A., and Oggier, M.: Retrieval of Snow Depth on Arctic Sea Ice From Surface-Based, Polarimetric, Dual-Frequency Radar Altimetry, Geophysical Research Letters, 50, e2023GL104 461, https://doi.org/10.1029/2023GL104461, 2023.

Willatt, R., Mallett, R., Stroeve, J., Wilkinson, J., Nandan, V., and Newman, T.: Ku- and Ka-Band Polarimetric Radar Waveforms and Snow Depth Estimation Over Multi-Year Antarctic Sea Ice in the Weddell Sea, Geophysical Research Letters, 52, e2024GL112 870, https://doi.org/10.1029/2024GL112870, 2025.

Wingham, D., Phalippou, L., Mavrocordatos, C., and Wallis, D.: The Mean Echo and Echo Cross Product from a Beamforming Interferometric Altimeter and Their Application to Elevation Measurement, IEEE Transactions on Geoscience and Remote Sensing, 42, 2305–2323, https://doi.org/10.1109/TGRS.2004.834352, 2004.